INTERNATIONAL DOCTORATE IN
ATOMIC AND MOLECULAR PHOTONICS

Dottorato Internazionale

Ciclo XXIX

COORDINATORE Prof. Roberto Righini

BRAIN VASCULATURE IMAGING WITH TWO-PHOTON AND LIGHT-SHEET MICROSCOPY

Settore Scientifico Disciplinare: FIS/03

Dottorando
Dott. Di Giovanna Antonino Paolo

Tutore
Prof. Pavone Francesco Saverio

Coordinatore
Prof. Righini Roberto

Anni 2013-2016

Contents

Part I

Introduction

Chapter 1

Brain imaging in wide scale

The brain is the most complex organ of our body. It allows us to interact with the external world integrating sensory input and producing adequate output to environmental changes. Understanding the mechanisms underlying brain function is a challenge currently ongoing and the cause of heavy financial investment. In 2005, IBM, in collaboration with the École polytechnique fédérale de Lausanne, launched the "Blue Brain Project" [1], later on, in 2009, the "Human Connectome Project" [2] started through a collaboration beetween the Laboratory of Neuro Imaging and Martinos Center for Biomedical Imaging at Massachussets General Hospital. Starting from 2013, the European Union has funded the "Human Brain Project"[3] which involves more than 90 research institutes and, in the same year, in the United States, the Obama administration announced the BRAIN initiative[4]. Moreover, in 2014, also Japan started its own initiative called Brain/MIND [5]. The funding of all these initiatives is justified by the difficulty to understand the physiology standing behind brain activity. The brain works as a whole, and a full comprehension of the processes governing its functions depends on a complete dissection of its anatomy, yet there are considerable structural differences in different part of the nervous system and a great interindividual variability. The connectivity of the brain can be analyzed at three quite distinct levels [6]:

1. Macroscopically, by examining images of the whole brain (or of large brain region) by magnetic resonance imaging (MRI), diffusion tensor imaging (DTI), magnetoencephalography, and electroencephalography.

2. Microscopically, by using optical techniques, which allow for subcellular resolution.

3. At ultrastructural level, using electron microscopy (EM), through which is possible to focus on fine morphological details with nanometric resolution.

While, the first approach enable fast analysis of the whole brain in living organisms, but with a quite coarse resolution (about one millimeter), the last one allows for the visualization of the finest morphological details, but only in small tissue sections. Optical techniques offer a trade-off between the two above. They give us the possibility to investigate morphological details below the micrometric scale, generally in areas of millimeters, within a depth of hundreds of microns at most. Recent methodological developments, have expanded potentiality of optical microscopy, enabling acquisitions of complete datasets of whole rodent brains. It is possible to distinguish two alternative approaches: one is based on tissue sectioning [7, 8], while the other one is based on tissue clarification. The latter allows for fast imaging of chemically-cleared, "transparent" mouse brains without the need for mechanical sectioning [9, 10, 11]. Both have been used for neuronal or vascular visualization, however without a complete analysis in the whole brain.

Neuronal activity is supported by an intricate network of blood vessels, which ensures the delivery of adequate levels of oxygen and nutrients for neuronal metabolism. Changes in blood supply inside any given brain area permits a dynamic allocation of resources based on metabolic needs. The regulation of blood flow according to increases or decreases in neuronal demand is known as neurovascular coupling [12]. This coupling is exploited for functional studies, in which blood flow changes are evaluated as surrogates of neuronal activity. Methodologies such as blood oxygenation level-dependent (BOLD) functional magnetic resonance imaging (fMRI), for instance, measure the level of blood oxygenation to extract information about neuronal activity. However, we do not have complete topological knowledge of the brain vasculature, especially of its capillary network, through which the exchange of substances and metabolites takes place. Questions about how these methodologies relying on blood oxygenation level reflect the underlying neuronal processing, and which areas of neurological activity correspond to the signals detected, are still open. Dissecting the topological features of brain vasculature at microscopic

scale will help to deliver a reliable interpretation of this data. If, on one hand, microscopic resolution is achievable with different techniques, the application of those same microscopy technologies over large volumes on the other hand is challenging. This problem is faced in this thesis presenting a methodological approach which has the potential of giving a complete comprehension of brain vasculature organization on a brain-wide scale. A thorough analysis of the vascular component is essential to step forward towards the comprehension of physiological processes through which the brain works. Besides, vascular changes are know to be correlated with neurological disorders, such as stroke [13], neoplasia [14] and dementia [15]. A methodology enabling detailed morphological vascular analysis on a whole brain scale would in this respect be of remarkable importance. In the next chapters of the introduction, a close up view on brain organization and imaging methodologies applied for brain research is presented.

Chapter 2

The architecture of the brain

The brain works as a whole, nevertheless it is composed of specialized areas managing specific functions. A complex neuronal network allows for the integration of processed informations between distinct areas and, extending out of the brain, it also make up the pathways by which sensory stimuli and motor outputs travel towards and from the brain. Alongside neuronal pathways, another network made of blood vessels guarantees the maintaining of adequate levels of oxigen and nutrients, essential for energy metabolism. Starting from the neuron, the unit forming the neuronal network, the next sections show a description of brain's anatomy with a special focus on the vascular component.

2.1 The brain's primary functional unit

The human brain contain approximately 86 billion neurons [16], which represent the fundamental units forming the neuronal network. Specialized structures identify these cells (fig.2.1). From the cell body, or soma, a large number of extensions called **dendrites** receive chemical messages from other neurons [18]. All the signals received are integrated in the soma and eventually conveyed in the form of electrical impulses thanks to another extension named **axon**. At the axon ending the signal is converted into a chemical message, consisting of molecules called neurotransmitters, which travel to the next neuron through a tiny gap known as **synaptic cleft**.
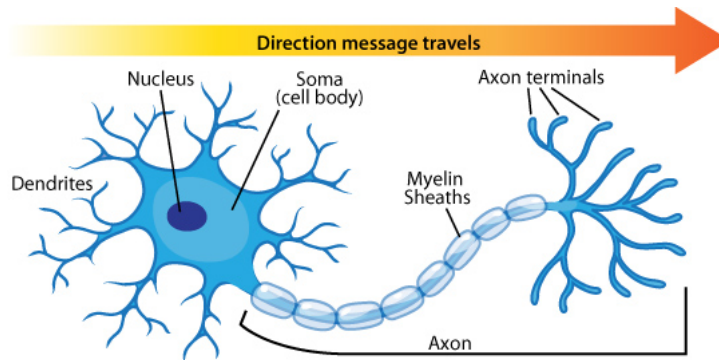
Figure 2.1: **Neuron structures** Messages coming from other neurons are received from the dendrites and integrated inside the cell body, which contains the nucleus as a separate cell compartment. If the sum of the messages received exceeds a threshold value, an action potential is generated. This new message in the form of an action potential runs along the myelinated axon towards the axon terminals. Image from [17]

When neurotransmitters contact the surface of a neuron downstream, they interact with membrane receptors which trigger a change of the electrical potential between the inside and the outside of the cell. The cell membrane potential at rest is around $-70mV$. Excitatory signals cause a depolarization of the cell, that means that the membrane potential is led towards more positive values. When the depolarization exceeds a threshold value, it elicits an **action potential** running along the length of the axon [19]. The action potential is sustained by the aperture of voltage-gated ion channels allowing for an inward current of Na^+, which is then stopped by a time-dependent closure of the same channels. A delayed aperture of voltage-gated potassium channels, which causes an outward flow of K^+, leads the membrane potential back to the resting value. At this point the sodium-potassium pumps work to restore the right concentration of Na^+ and K^+ inside the cell.

The depolarization has self-sustained properties and propagates from a region to another along the axon. A myelin sheath wrapped around the axon speeds up this process considerably. It works as an electrically insulating layer, which is interrupted in several points, called nodes of Ranvier, where the ions exchange take place. Hence the impulses propagate by saltatory conduction jumping from a gap in the myelin sheath to the next [20]. The cells producing myelin and wrapping themselves around the axons are oligodendrocytes in the central nervous system (CNS) and Schwann cells in the peripheral nervous system. Considering

the distance each signal has to cover to reach its target, the presence of myelin is of primary importance. An axon in human, for instance, can reach up to one meter of length in the case of a neuron extending from the spinal cord to a muscle of the foot.

The axon divides into several branches in order to transmit signals to different neurons simultaneously. The distal terminations of the axon's branches are called presynaptic boutons. These sites store the synaptic vesicles containing neurotransmitters, which are released as a consequence of a biochemical cascade triggered by the activation of voltage-gated calcium channels when the depolarization reach the end of an axon [21]. Each neuron is able to receive and integrate thousands of signals. The dendrites protruding from the soma present an elevated number of ramifications and contain multiple specialized protrusion, the **dendritic spines**, which make synaptic contacts. In some cases the degree of dendritic ramification is as high as to generate up to 100'000 input on a single neuron [22].

The activity of neurons is supported by an heterogeneous population of non neuronal cells present in the nervous system and indicated together as glial cells. In addition to the above mentioned oligodentrocytes, in the CNS the population of glial cells include astrocytes, ependymal cells and microglia. The astrocytes interacting with endotelial cells form the blood brain barrier, which controls the flux of substances from the blood stream into the brain extracellular fluid, and participate in the regulation of the local blood flow [23]. Other roles for this abundant population encompass the maintenance of the extracellular ion balance [24], metabolic support [25], modulation of synaptic transmission [26], promotion of the myelination carried by oligodendrocytes [27], uptake and release of neurotransmitters [28], and generation of the glial scar during brain repair [29]. The ependymal cells make the epithelium layer of the ventricular system of the brain and contribute importantly to the flow of cerebrospinal fluid (CSF) [30]. The microglia, instead, act as immunoeffector cells and scavengers for plaques and potentially deleterious debris [31].

2.2 Anatomy of the brain

Anatomically the brain can be divided into three basic regions [18]: the **hindbrain**, the **midbrain**, and the **forebrain**. The hindbrain contains three distinguishable structures: The medulla oblongata, the pons, and the cerebellum. The **medulla oblongata** lies directly above the spinal cord and form a continuum with it. Vital autonomic functions, such as digestion, breathing, and the control of heart rate are directed in this brain area. The **pons** is located above the medulla and in front of the cerebellum. It conveys information about movement from the cerebral hemispheres to the cerebellum. The **cerebellum**, placed behind the pons and connected with it by the cerebellar peduncles, modulates the movements and is involved in the learning of motor skills. Rostrally to the pons, the midbrain controls many sensory and motor functions, including eye movements and the coordination of visual and auditory reflexes. The midbrain, pons and medulla oblongata constitute the so called **brain stem**.

The forebrain is the largest part of the brain and can be divided into two main parts, the **diencephalon** and the **cerebral hemispheres**. The diencephalon consist of the thalamus and the hypothalamus. The first relays sensory and motor signals to the cerebral cortex, while the second regulates autonomic, endocrine, and visceral functions. The cerebral hemispheres comprise the cerebral cortex, the basal ganglia, the hippocampus, and the amigdaloid nuclei (fig.2.2a). The cerebral cortex is the outer part of the brain. Looking at its surface four lobes are evident for each hemisphere: the frontal lobe, the parietal lobe, the temporal lobe and the occipital lobe (fig.2.2b). Numerous neuronal cell bodies are present making up the gray matter of the brain, visually different from the area beneath, (the white matter), which is composed mainly of long-range myelinated axons. The cerebral cortex play a key role in memory, attention, perception, awareness, thought, language, and consciousness. The basal ganglia is a collective term for a set of structures in the basal forebrain [34]. In this set we can discern the striatum, which is the largest component, the pallidum, the substanzia nigra and the subthalamic nucleus. They participate in regulating motor performance. The hippocampus plays a critical role in memory storage and it also give a significant contribution to understand spatial relations within the environment [35]. The amygdaloid nuclei
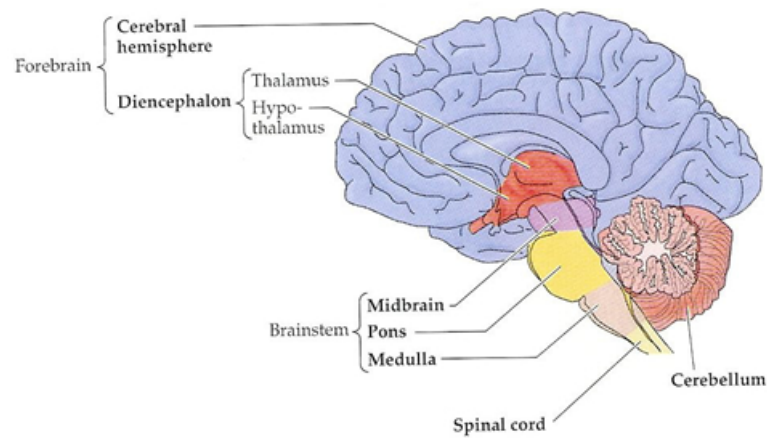
(a) Brain structures
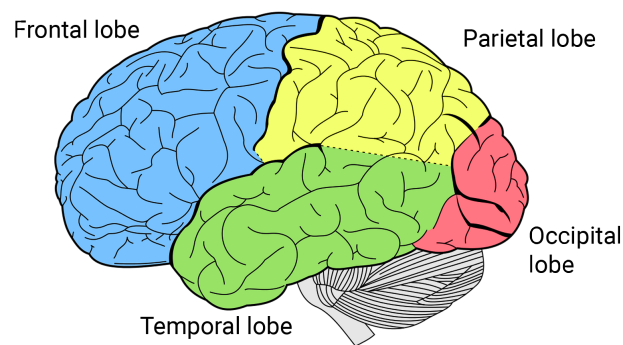
(b) Lobes of the cerebral cortex

Figure 2.2: **Anatomy of the brain** (a) The most prominent brain structures and their subsections are shown. The forebrain is divided into cerebral hemispheres and diencephalon. The midbrain along with the pons and the medulla oblongata (so with the hindbrain excluding the cerebellum) form the brain stem, structurally continuous with the spinal cord. (b) Representation of the four cortical lobes of the brain: the frontal, parietal, temporal, and occipital. Both the left and right hemispheres have one of each cortical lobe. While the frontal lobe is separated from the temporal and the parietal lobes by fissures in the brain tissue, the other lobes are only separated by imaginary lines. (a) from [32]. (b) from [33].

is a critical center for coordinating behavioral, autonomic and endocrine responses to environmental stimuli, especially those with emotional content.

All vertebrates share common basic components. Studies on different animals can then give insights about humans, especially those carried on evolutionary close species. Mammalian animal models, such as mouse, are extensively studied for understanding the key principles of brain function (fig. 2.3). The most obvious difference between the brains of mammals and other vertebrates is in terms of size. On average, a mammal has a brain roughly twice as large as that of a bird of the same body size, and ten times as large as that of a reptile of the same body size [36].
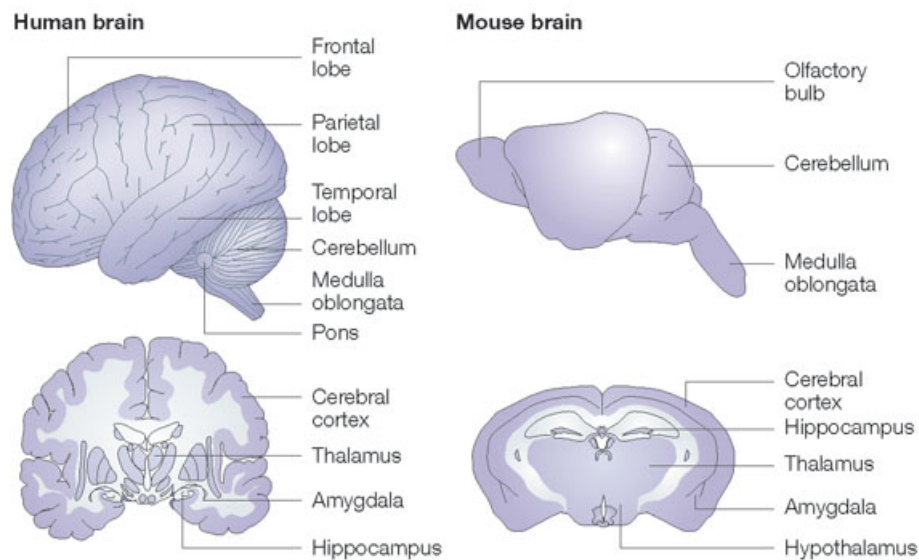
Figure 2.3: **Comparison between human and mouse brain anatomy**. Many brain structures like cerebral cortex, hippocampus, thalamus, amygdala, hypothalamus, cerebellum, and medulla oblongata are evolutionary conserved from mouse to human. Fig. from [37].

Inside the brain, it is possible to observe four interconnected cavities called ventricles. These are filled with cerebrospinal fluid (CSF), which flows from the ventricles through the whole brain delivering nutrients and washing out waste, such as neurotoxins and protein aggregates [38]. The brain does not directly take contact with the skull, but it is surrounded by three membranes called meninges.

The outer is the dura mater, that adhere directly to the bone and envelops the other meningeal layers. The other internal layers are the arachnoid and the pia mater, the last one being the most internal membrane [39]. The arachnoid is linked to the pia by arachnoid trabeculae that span the subarachnoid space filled with CSF produced by choroid plexi.

2.3   Brain vasculature

The brain is higly sensitive to insufficient blood supply. When the blood supply is interrupted, neurons stop firing within seconds and die within minutes [40]. Therefore the cerebral blood flow needs to carry oxygen and nutrients efficiently to the nervous system and take away carbon dioxide, lactate and other metabolic products. The CNS receives blood by means of two sets of vessels: the right and left **internal carotid arteries** (ICAs) and the right and left **vertebral arteries** (VAs) [41] (fig.2.4). While the ICAs are responsible for the anterior circulation of the brain, the VAs account for the posterior circulation. The VAs merge together becoming the **basilar artery**(BA). In humans the BA connects to the ICAs forming a structure known as **circle of Willis** (fig.2.5). Since the arteries are joint to form a circle, if one of the main arteries is occluded, for example the carotid artery, the distal smaller arteries that it supplies can receive blood from the other upstream arteries (collateral circulation). This happens in particular when, due to atherosclerosis, slow and progressive occlusion occurs and the vessels have time to expand allowing the passage of a greater amount of blood [41].

Mouse models are extensively used for studying brain circulation and evaluating damage following blood flow interruption [43]. However, differences in blood vessel connections have to be taken into account. The mouse circle of Willis for example does not form a closed circuit, since there are no connections between the BA and the ICAs [44].

In humans, the **middle cerebral artery** (MCA) is the largest branch of the ICA. It branches out onto the surface of the frontal, parietal and temporal lobes and feeds most of the cortex and the white matter. Further branches of the MCA dive deep into the brain feeding the basal nuclei. In mouse, instead, the ICA drains chiefly into the olfactory artery (OlfA). These differences are consistent with the
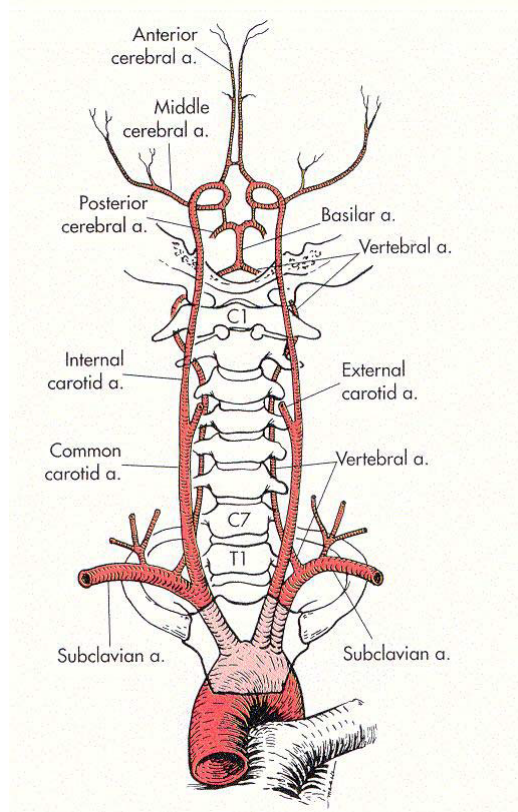
Figure 2.4: **Origin of the arteries supplying the brain** Branching respectively from the common carotid arteries and the subclavian arteries, the ICAs and the VAs carry blood towards the brain circulation. Fig. from [42]

mouse being a nocturnal carnivore that lives on olfactory informations in contrast to the humans that live diurnally and depends on visual and auditory informations [44].

The arteries running on the surface of the brain, above the pia mater, are called pial vessels (fig. 2.6). They give rise to smaller arteries that eventually penetrate into the brain tissue originating the penetrating arterioles [45]. As penetrating arterioles descend into the cortex, they gradually ramify until they form the capillary network [46, 47]. From this network originates the venular system, similar to the arterial system, which guide the blood out of the brain.

The veins of the brain may be divided into two sets, cerebral and cerebellar [51]. The **cerebral veins** are divisible into an external and internal group according to whether they drain the outer surfaces or the inner parts of the hemispheres
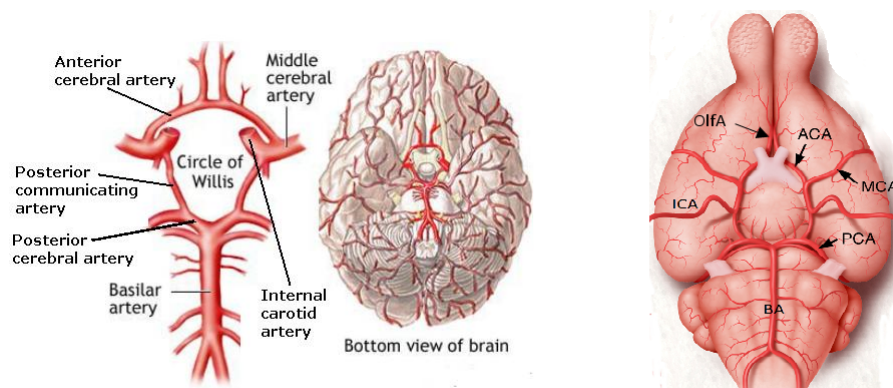
human circle of Willis   mouse circle of Willis

Figure 2.5: **circle of Willis** Bottom view of the circle of Willis in human (left) and mouse (right). In human the circle of Willis is composed of arteries connecting the basiliar artery (BA) to the ICAs. The components of this circle are the ICAs, the anterior cerebral arteries (ACAs), the posterior communicating arteries, and the posterior cerebral arteries (PCA). In mouse, the BA and the ICA domains are discrete and independent units of blood supply. Image on the left from [48]. Image on the right adapted from [49].

(fig.2.7a 2.7b). Large veins channels called sinus receive blood from the internal and external veins. Via a confluence of sinuses, the drained blood is directed toward the sigmoid sinuses and finally to the jugular veins.

The **cerebellar veins** are placed on the surface of the cerebellum, and are categorized into two sets, superior and inferior. The superior cerebellar veins end in the straight sinus, the inferior cerebellar veins end in the **transverse**, and
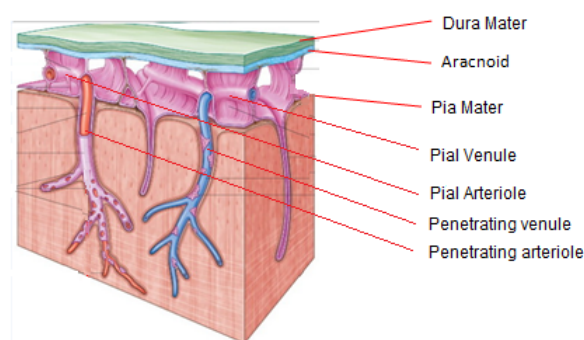
Figure 2.6: **Pial vessels** Standing above the pia mater, pial vessels extend branches into the parenchyma forming penetrating arterioles and venules, which are connected by a capillary network (not shown). Adapted image from [50].

occipital sinuses. By means of a connecting point called confluence of sinuses they end in the **sigmoid sinus** which represent the superior tract of the internal jugular vein.

Although the connectivity of the major brain vessels is known, we do not have detailed information about the intricate capillary network, by which the exchange of metabolites takes place. Thanks to continuous advances in microscopy techniques we are now able to analyze the microvasculature on larger portions of tissues and extend our knowledge about the microcirculation of the brain.
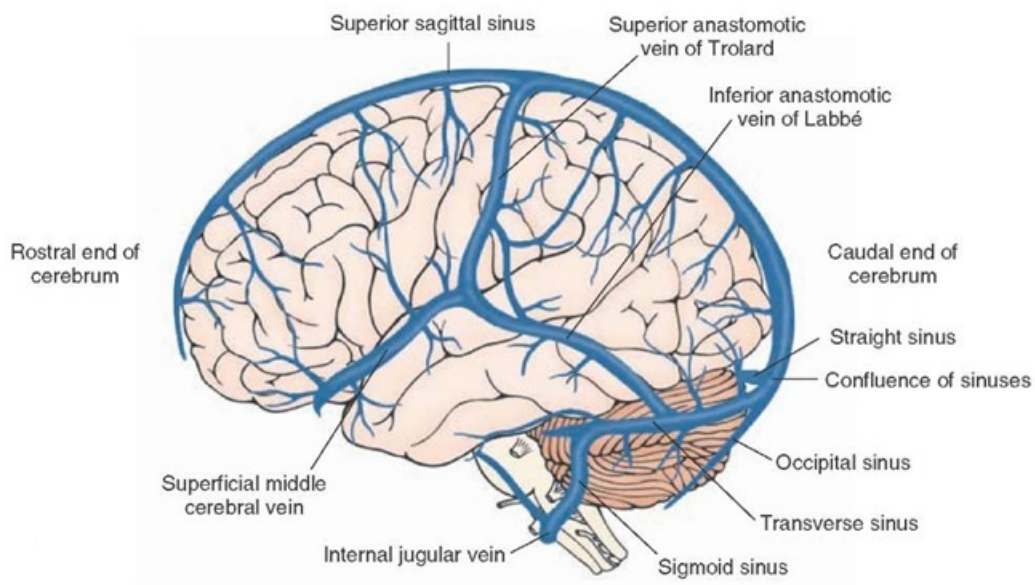
(a) Veins of the outer surface of the brain
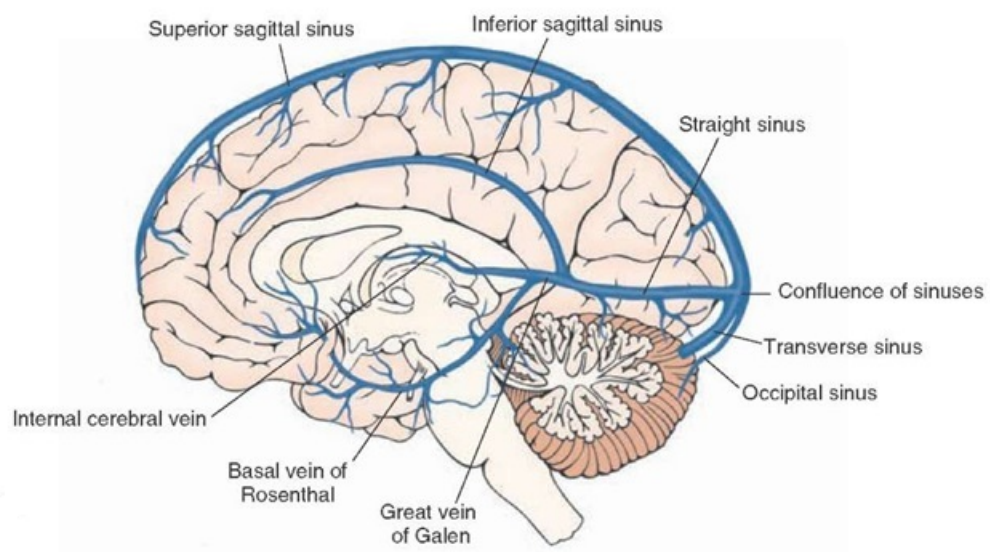
(b) Veins of the inner part of the brain

Figure 2.7: **Human venous system** The cerebral venous system can be divided into superficial veins (a) and deep veins (b). (a)The superficial venous system comprises the sagittal sinuses and cortical veins, subdivided into superior, middle and inferior. (b) The deep venous system consist of lateral sinuses, sigmoid sinuses, straight sinus and draining deep cerebral veins. Images from http://ranzcrpart1.wikia.com/wiki/Venous

Chapter 3

Fluorescence optical microscopy

The invention of the microscope has brought a notable evolution in medicine by making visible fine components of our body. A great number of optical microscopy techniques have been developed from then improving our capability to explore the composition of organs and tissues. In particular, fluorescence optical microscopy has introduced the possibility to highlight specific elements of interest in biological specimens labeled with fluorescent probes. This chapter describes the features of fluorescence microscopy and the working principles of two microscopy techniques, two-photon fluorescence microscopy (TPFM) and light sheet fluorescence microscopy (LSFM). The applicability of these two techniques expanded after the introduction of new chemical treatments which are able to make biological tissues optically transparent. The last section is devoted to the description of these treatments, named "clearing methods".

3.1   Fluorescence microscopy

The spontaneous emission of light following light absorption by a molecule, with a typical emission rate of 10^8 s^{-1} is termed fluorescence, and molecules showing fluorescence emission are known as fluorophores. A characteristic of fluorescence is the larger wavelength of the emitted radiation with respect to the absorbed one. This phenomenon, known as Stokes shift, represents a distinctive feature of fluorescence and is caused by a loss of energy before emission. The fluorescence process
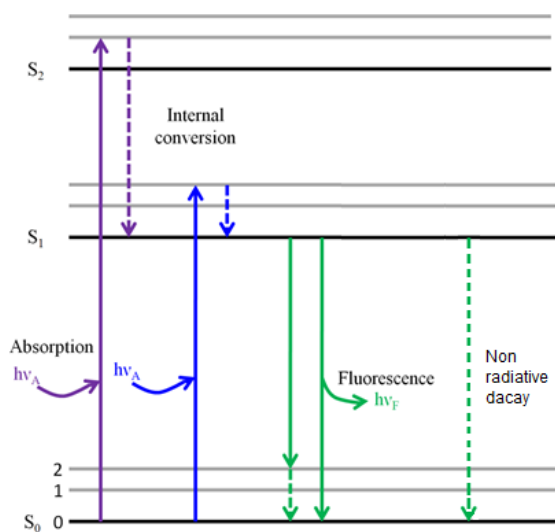
Figure 3.1: **Jablonski diagram** The violet and the blue arrows represent two examples of electronic transition upon absorption of photons. A fast non-radiative process called internal conversion brings the molecule down to the lowest vibrational level of S_1 before fluorescent emission. The green arrows depict the decay to the ground state S0 with photon emission (continuous line), or by means of a non radiative process (dotted line). This transition brings the molecule to one of the vibrational states of S_1.

is usually illustrated by a Jablonski diagram [52] (fig.3.1). A typical Jablonski diagram shows the electronic states of a fluorophore as horizontal lines, indicated in fig.3.1 as S_0, S_1 and S_2. Each state can exist in a number of vibrational energy levels depicted as 0, 1, 2. The transition between states are depicted as vertical lines. Whatever is the vibrational level of the molecule after light absorption, it rapidly relaxes to the lowest vibrational level of S_1 [52]. This process is named internal conversion and occurs within 10^{-12} s. Exceptions exist, for instance, some molecules are known to emit from the S_2 level, but such emission is rare and generally not observed in biological molecules. The return to the ground state S_0 from S_1 occurs with the emission of electromagnetic radiation, which, because of internal conversion, has a lower energy (or longer wavelength) with respect to the excitation light. Furthermore fluorophores generally decay to high vibrational levels of S_0, resulting in a further loss of energy. Non radiative transitions from S_1 to S_0 can also happen, decreasing the rate of fluorescence emission.

Two important characteristics of fluorophores are the fluorescence lifetime and the quantum yield. The fluorescence quantum yield, Q, is the ratio of the number of photons emitted to the number absorbed. This is given by

$$Q = \frac{\Gamma}{\Gamma + k_{nr}} \qquad (3.1)$$

Where Γ represent the emissive rate of the fluorophore, and k_{nr} the rate of non radiative decay. Substances with larger quantum yield, such as rhodamines, display brighter emission. The fluorescence lifetime is instead defined by the average time the molecule spends in its exited state prior to returning to the ground state. It can be described as

$$\tau = \frac{1}{\Gamma + k_{nr}} \tag{3.2}$$

The intensity of fluorescence can be decreased by a variety of processes collectively termed quenching. Collisional quencing, for instance, is due to contacts of the fluorophore with other molecules. In such scenario, the energy absorbed is dissipated by collisions, thereby increasing k_{nr}. In the case of static quenching, the fluorophore reacts with another molecule forming a nonfluorescent complex.

3.2   Optical resolution

The resolution of an optical microscope is defined as the shortest distance between two points on a specimen that can still be distinguished as separate entities. Image resolution is limited by diffraction, a phenomenon occurring when light encounters obstacles, or limiting apertures, in its path. The three-dimensional diffraction pattern of light emitted from a point source in the specimen is called point spread function (PSF). Fluorescent objects that are closer than the Full Width at Half Maximum (FWHM) of the PSF cannot be distinguished (fig.3.2). The Rayleigh criterion states that two point sources are regarded as just resolved when the maximum of the PSF of one point coincides with the minimum of the other [53]. This distance (r_{min}) is called Rayleigh limit. If the distance is greater, the two points are well resolved, while if it is smaller, they are regarded as not resolved. The Rayleigh limit for an optical microscope is given by the Abbe formula:

$$r_{min} \approx \frac{0.6\lambda_0}{NA} \tag{3.3}$$

where NA is the numerical aperture of the lens, defined as

$$NA = n \times sin\theta \tag{3.4}$$

where n is the refractive index of the medium and θ is the half-angle of the maximum cone of light that can be collected by the microscope objective [54].

In optical systems, the fluorescent light emitted by the sample is collected by means of detectors which are unable to distinguish light coming from different planes. The contribution of fluorescent molecules excited in out-of-focus planes results in image blur. To reduce the contribution of out of focus light, one solution is to analyze just a thin section of tissue. This approach requires the sample to be cut, generally in slices with a thickness of tens of microns using a specific instrument called microtome. Other approaches, however, have been developed to avoid mechanical sectioning of the sample. One of these is called confocal microscopy [55]. In confocal microscopes, the out of focus light is rejected by means of a pinhole placed in front of the detector, which prevents the light coming from out-of-focus planes to be collected. The capability of getting separated images of different planes inside tissues without the need of physical removal, but instead using an optical approach, is called optical sectioning. Two other microscopy techniques, two-photon fluorescence microscope (TPFM) and light sheet fluorescence microscope (LSFM), achieve optical sectioning by confining the excitation of fluorescence in one plane. The TPFM and LSFM working principles are described in more detail in the following chapters.
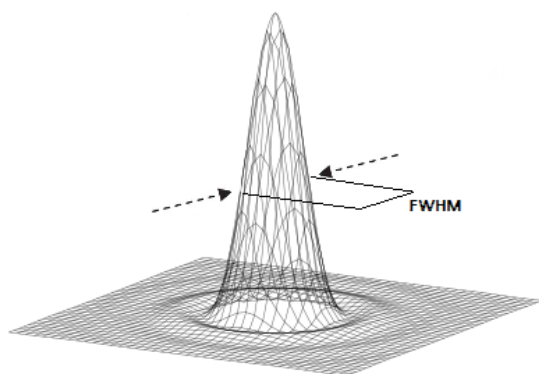

Figure 3.2: **Point spread function** The FWHM of the PSF determines the minimal distance between two objects in order to distinguish them as two different entities ccording to Rayleigh.

3.3 Two-photon excitation

Two-photon absorption was first predicted by Maria Göppert-Mayer in 1931 [56, 57]. She proposed that a molecule should be capable of absorbing two photons in the same quantum event within 10^{-16}-10^{-17}s. Because this is a rare event at ordinary light intensity, it was only in the 1960s, after the development of laser sources, that the prediction could be experimentally verified [58]. The first application of two-photon excitation to fluorescence microscopy was presented at the beginning of the 1990s by Denk and collegues [59]. Multiphoton processes such as two-photon excitation are termed "nonlinear" because the rate at which they occur depends nonlinearly on intensity. Since TPFM requires the simultaneous absorption of two photons (within $\sim 10^{-16}$s) to excite the molecule, the fluorescence signal depends on the square of the illumination intensity [57]. To achieve a reasonable excitation efficiency, typical TPFM systems focus the excitation photons into a tiny volume using a high numerical aperture (NA) objective [60, 57]. However, focusing alone is not enough to make two-photon microscopy practical. A very high laser power would be in fact required for an appreciable fluorescence emission. To generate enough fluorescence for imaging while keeping the average power relatively low, a pulsed laser is used. Pulsed lasers increase the probability of two-photon interactions. The most common ones are titanium sapphire lasers, which produce $\sim$80 million pulses per second, with a pulse duration of $\sim$100 fs.

Away from the focal plane, the TPE probability drops off rapidly so that no appreciable fluorescence is emitted. This feature has important consequences. First of all, it avoids using a pin-hole to exclude out-of-focus light [60, 57]. Since the pinhole partially rejects also photons coming from the focus plane, the signal detected with TPFM is increased with respect to confocal microscopy. Second, continuous excitation of the same molecule leads to fluorophore damage, and results in a loss of fluorescence emission. This phenomenon, called photobleaching, is considerably reduced in TPFM, because fluorophores located away from the focal spot are not excited.

Since the total energy transfered to a molecule is given roughly by the sum of two photons, higher wavelength, typically in the infrared spectrum (IR), are used for excitation. IR wavelengths are less scattered than visible light. Thus IR

radiation is capable of penetrating deeper inside biological tissues, giving a further advantage for three-dimensional reconstruction. Because of the non-linearity of the process, only a tiny spot inside the tissue emits fluorescence. Fluorescence signal from the remaining volume which the laser passes through is completely avoided, resulting in lower background fluorescence. The maximum depth achievable with TPFM is about 800 μm in living animal and around 200 μm in fixed tissues [61, 62], a considerable improvement compared to less then 100 μm of depth achievable using confocal microscope. Moreover, the use of IR wavelength results in less phototoxicity in the case of *in vivo* imaging. [58].

The fluorophores which undergo two-photon excitation display the same emission spectra and lifetime as if they were exited by one-photon absorption [52]. Indeed, although the fluorophore may be placed into different excited states, they emit from the same electronic state, independently of one or two-photon excitation process. A Jablonski diagram describing two photon excitation is shown in fig. 3.3.
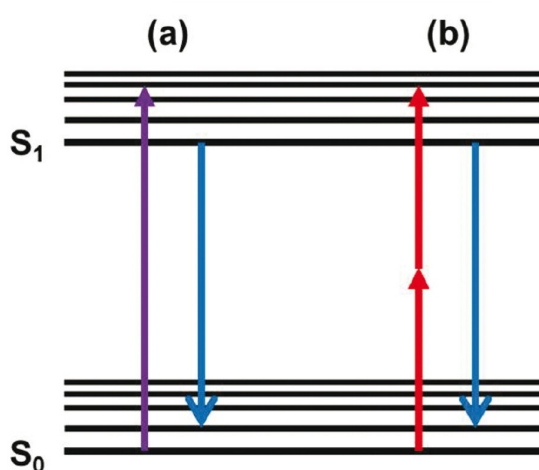
Figure 3.3: **Jablonski diagram showing one- and two-photon excitation** (a) In one photon excitation a single photon having a specific wavelength is responsible for the transition to an higher molecular state. (b) In two-photon excitation the transition to the excited state is caused by the additive effect of two photons. The emitted light (blue arrows) is not depending on the mode of excitation. Image from: [60].

In two-photon fluorescence microscopy, as in conventional laser-scanning confocal microscopy, a laser is focused and raster-scanned across the sample. The image consists of a matrix of fluorescence intensity measurements made by the detector while the laser sweeps back and forth in the sample. The scanning mode makes the image acquisition slower than traditional wide field methodologies. Hence, although its capability of imaging deep into specimens, the imaging of large volumes,

such as whole mouse organs, is time consuming. For whole organ reconstruction, a different methodology called light sheet microscopy has been recently applied.

3.4 Light-sheet microscopy

The principles of light-sheet microscopy were first described by Richard Adolf Zsigmondy in a paper published in 1903 [63, 64]. However it was only in 1990s that it was used for imaging of fluorescent biological samples [65]. Light-sheet fluorescence microscopy (LSFM) uses a laser light-sheet for illumination, i.e. a laser beam which is focused only in one direction using a cylindrical lens. In LSFM, the sample is illuminated perpendicularly to the detection axis, letting the above and below planes not subjected to the excitation light (fig.3.4). The axial reso-
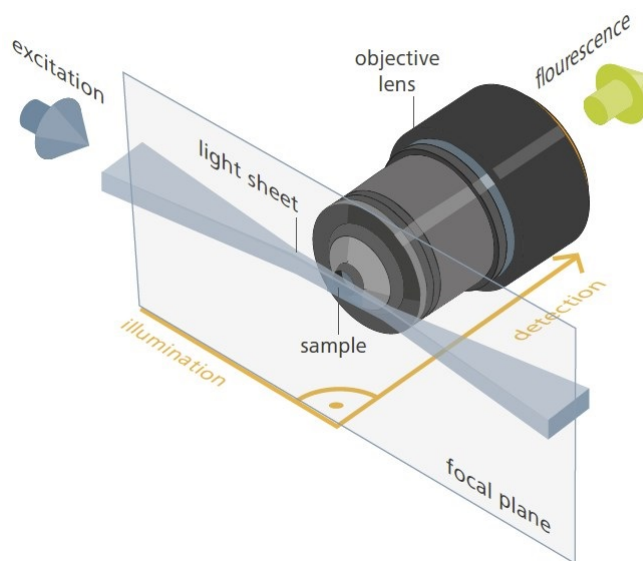
Figure 3.4: **Light-sheet microscope** A light sheet is focused inside the sample generating a plane of excitation. The fluorescence emitted is collected perpendicularly to the illumination path by an objective lens. Image adapted from Olaf Selchow and Jan Huisken: *Light sheet fluorescence microscopy and revolutionary 3D analysis of live specimens,* Photonk international, 2013.

lution of this technique is depending on the thickness of the light sheet created,

which is typically a few micrometers. The optical sectioning offers the advantage of minimizing fluorophore bleaching and phototoxic effects. The fluorescence light emitted is collected perpendicularly with a microscope objective, and projected onto a CCD or a cMOS camera. Since an entire plane is illuminated at any time, this approach is considerably faster than laser scanning microscopy. This high speed acquisition makes LSFM suitable for reconstructing volumes of tissue which are prohibitive in terms of time using confocal or TPFM. However, this technique requires transparent samples to acquire images at depth. This limitation has been addressed with the development of methodologies able to render tissues optically transparent, collectively called "clearing methods". A number of different solutions also have been developed to improve resolution and reduce artifacts and aberrations due to the inhomogeneity of the sample. The most crucial of these encompass the implementation of structured illumination [66], the replacement of a classical Gaussian beam with Bessel beam for light-sheet generation [67], the introduction of confocal light sheet microscopy [68, 69], and the use of two light sheets that combined illuminate the specimen from opposite sides [70]. The coupling of LSFM with clearing methods has boosted the study of neuronal connectivity in mouse models on a brain wide scale [71].

3.5 The advent of clearing methods

The possibility to collect images deep inside tissues and organs with optical techniques is principally prevented by light scattering. Scattering occurs when the direction of light is deviated by refractive index (RI) inhomogeneities during light propagation [72]. The RI is described as $\frac{c}{v}$, where c is the speed of light in vacuum and v the phase velocity of light in the medium. Since biological tissues are made of components with different RIs, light is deviated along its path inside the sample. This deflection hampers photons to reach the common focus for excitation of fluorescent molecules (fig. 3.5a) and, at the same time, hinders the detection of the emitted fluorescence (fig. 3.5b). To overcome this limitation, biological samples are treated with solutions able to homogenize the RI inside tissues, called clearing agents.

The first report on clearing opaque biological samples dates back to 1914 with

(a) Excitation path   (b) Emission path
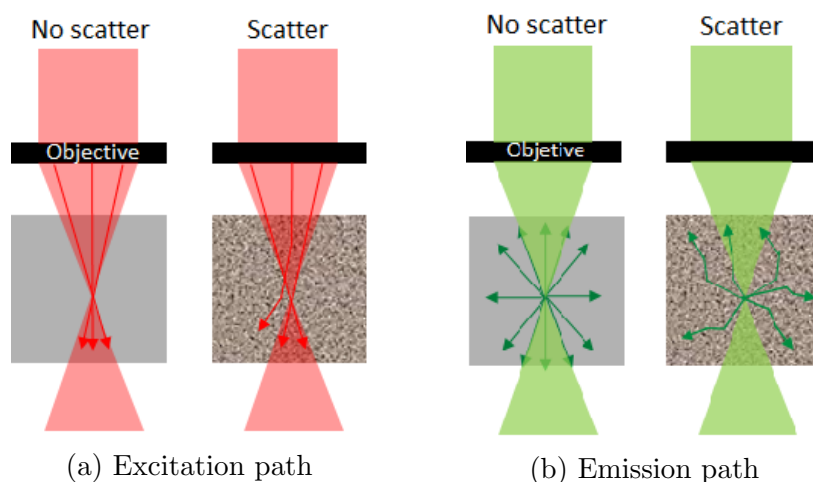
Figure 3.5: **Scattering inside tissues** (a) In non-scattering samples, light rays are all directed towards the focal spot. In presence of scattering, the percentage of photons reaching the focal spot decreases. (b) In absence of scattering, the fluorescence propagates uniformly in all directions. In scattering samples, the amount of photons detected is reduced.

a book published by the German anatomist Walter Spalteholz [73]. In order to obtain transparent preparations, he tested numerous organic solutions and found a mixture of benzyl alcohol and methyl salicylate to be most effective for clearing large specimens. Later on, a modified clearing solution called "Murray's clear" was used for embryo imaging [59, 74]. This solution was applied in combination with LSFM for imaging of strongly fluorescent biological specimens, including whole mouse brain [11]. However, this mixture markedly reduces the fluorescence signal. This reduction is mainly due to the dehydration step which samples must undergo, being Murray's solution immiscible with water. In the attempt to reduce the fluorescence quenching observed, another screening found that dehydration with tetrahydrofuran, instead of alcohol, and incubation with dibenzyl ether, increased the fluorescence detected [75]. All these procedures are based on organic solvents, thus making tissue dehydration a necessity. The dehydration process is responsible for the loss of fluorescence reported. Moreover, the sample becomes strongly shrunk with respect to its original size. A method called iDISCO [76] introduced the possibility to combine organic-based clearing with immunostaining, thereby eliminating the need of fluorescence preservation where immunostaining

approaches can be a valid alternative.

A considerable improved fluorescence preservation was obtain by the development of water-based optical clearing, among them Sca/e [77], seeDB [78], ClearT [79], and CUBIC [20]. Each of these methods presents significant drawbacks, such as long incubation time, introduction of structural alterations, incompatibility with immunostaining, poor clearing capability of large samples, or difficult handling procedures. Moreover the transparency achieved is less compared with the use of organic solvent.

A different approach based on tissue trasformation has obtain a great success for its capability of rendering whole mouse brains highly transparent without flurescence quenching and facilitating dye penetration inside the tissue [80]. This approach, termed CLARITY, works by removing lipids, which represent the cellular component mainly responsible for light scattering, while preserving the protein component. This is achieved by a selective crosslink of proteins with a hydrogel matrix of acrylamide and formaldehyde created inside the brain. Since the lipids are excluded from the mesh of hydrogel, they can be selectively washed out using a soapy solution. The process can be expedited by the application of an electric field pushing the negatively charged micelles containing lipids away from the tissue (fig.3.6). The hydrogel-hybridized form of the brain deprived of lipids is then incubated in a refractive index matching solution for imaging. However the extremely high cost of this solution, called FocusClear^{TM}, limitates the use of CLARITY for routinely applications. A valid alternative to FocusClear^{TM} consists in a solution of Thiodiethanol (TDE) in phosphate buffer saline (PBS) [9]. CLARITY-TDE has demonstrated to be effective in clearing whole mouse brain for LSFM and to be compatible with immunostaining. The use of TDE is not confined to its application with CLARITY. It can be applied to fast clearing of brain slices or portions, such as hyppocampus, in order to achieve organ reconstructions by serial sectioning methodologies. The possibility to finely change the RI of TDE-PBS solutions makes it a versatile clearing agent suitable for investigation of different biological tissues with multiple imaging modalities.

Tissue clearing makes investigations of fine biological structures in a wide scale possible. To fully exploit this potential, high throughput methodologies with high resolution are required. LSFM seems well suited for this purpose thanks to its
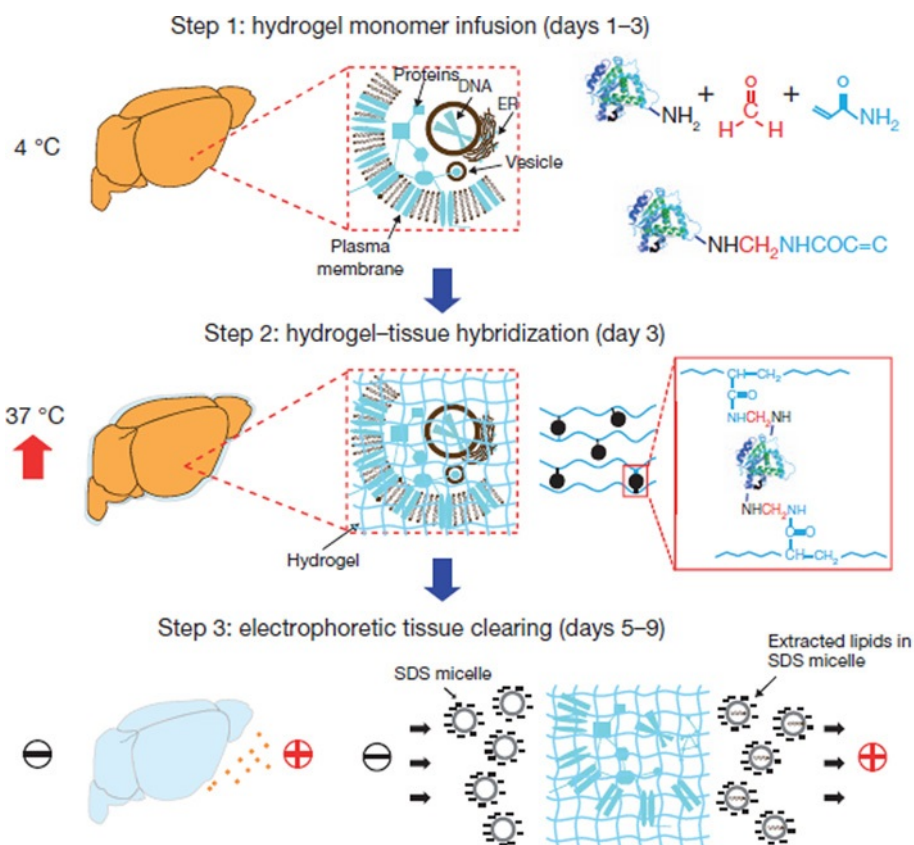
Figure 3.6:   **CLARITY** A mouse brain is incubated in a solution of acrylamide monomers (blue) and formaldehyde (red). Amminic groups allow proteins to covalently link the monomers. The polimerization triggered by heating creates a hydrogel mesh in which proteins are included. Finally the application of an electric field across the sample permits the active transport of micelles containing lipids out of the brain. Image from [80].

micrometric resolution coupled to a fast image acquisition rate. Brain research is one of the fields which can take more benefits from these advancements. Alongside neuronal connectivity, the brain vascular network has also been explored with these approaches.

Chapter 4

Brain vasculature imaging

The investigation of the brain's vascular component through imaging analysis can be accomplished with an increasing number of methodologies. We can distinguish two groups based on the possibility to apply them in living animal, or in other words *in vivo*. *In vivo* technologies such as magnetic resonance imaging (MRI) or computed tomography (CT) represent important diagnostic means to identify abnormalities or evaluate vessels occlusions in humans. On the other hand, they are profoundly wanting on a microscopic level. Nevertheless, because of their minimal invasiveness, experimental approaches have been developed in order to improve the resolution of these technologies for *in vivo* investigations in animal models. Optical microscopy, instead, offers the possibility to investigate brain vasculature in a sub-micrometric scale. Since optical microscopy does not hold the property of visualizing internal structures, surgical procedures such as craniotomies, implantation of cranial window, or skull thinning are executed in animals to expose brain portions for *in vivo* studies. In any case, only superficial brain layers are accessible.

In the attempt of getting a detailed topological organization of brain vasculature on a wide scale, optical strategies, or other approaches, are applied in excised organs, namely *ex vivo*. This chapter takes a view of the methodologies applied both *in vivo* and *ex vivo* in the pursuit of a fine understanding of vasculatur morphology inside the brain.

4.1 *In vivo* brain vasculature imaging

Different *in vivo* brain vasculature imaging methods are available, each with different temporal and spatial resolution, field of view, and invasiveness. Each of these technologies represents a trade-off between the above parameters. For whole-brain acquisition, approaches based on MRI or CT are typically adopted, while optical microscopy instead, is more suited for the analysis of small brain regions with higher resolution. *In vivo* whole brain and optical modalities are laid out separately in this section.

4.1.1 *In vivo* whole brain methodologies

MRI and CT yield images of internal body structures without the need of surgical intervention. For this reason they keep a relevant role in the diagnosis of different pathologies, among them vascular impairments. In addition to diagnostic use in humans, these methodologies have been applied in small animals to obtain full datasets of whole brain vasculature. Time of flight angiography (TOF), for instance, is a non-invasive MR method which allows the visualization of blood flow in whole mouse brains with a resolution close to 1 mm [81]. In order to visualize smaller vessels, a contrast agent injected into the blood flow is needed. With contrast-enhanced MRI, vessels with a diameter down to $\sim$100 μm have been detected in whole rodent brain[82].

A resolution of about 40 μm, has been instead achieved with microscopic computed tomography (μCT), using a contrast agent and applying adequate radiation doses [83]. μCT is based on the same underlying physical principle of CT, but achieves microscopic resolution by taking hundreds of 2D projections from multiple angles around the animal [84]. Both MRI and CT offer the possibility to acquire images of the whole brain in living animals with minimal invasiveness, although care has to be taken in the case of CT about the level of ionizing radiations, which are hazardous to health. Recently another approach based on ultrafast doppler tomography (UFD-T) has been proposed for whole brain imaging of blood vessels in rodents [85]. This technique requires skull removal in rats, but could potentially be performed through the skull in mice. Thanks to a tomographic scanning
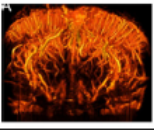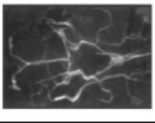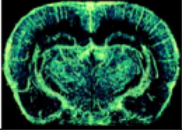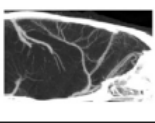
	Whole brain & *in vivo*			
In vivo imaging Modality	UFD-T	MRI (TOF)	MRI (contrast)	µCT (low dose)
Depth	Whole brain	Whole brain	Whole brain	Whole brain
Resolution	~100 µm	~mm	~100 µm	~40 µm
Acquisition time	20 min	~5-30 min	76 min	50 min
Need for contrast agents	No	No	Yes	Yes
Invasiveness	Skull removed or thinned*	No	Contrast injection	Contrast injection
Portability	++	---	--	-
Example	(Demené et al., 2015)	(Beckmann et al., 1999)	(Lin et al., 2009)	(Starosolski et al., 2015)

Figure 4.1: **Whole rodent brain angiography** A schematic representation of whole brain methodology for vasculature imaging is given. Each technique has its own advantage in terms of resolution, acquisition time or invasiveness. TOF-MRI is an absolutely non invasive method, but offers a lower spatial resolution (∼mm). The use of a contrast agent injected into the blood enhances the resolution achievable in MRI and CT. UFD-T is more invasive, but presents advantages in terms of temporal resolution. Adapted from [85].

approach requiring successive translation/rotation scans, a voxel dimension of 100 μm^3, with a temporal resolution of 10 ms has been obtained in whole rat brain. The main advantage of UFD-T over CT and MRI modalities is its temporal resolution. Dynamic changes of blood volume and blood flow speed can indeed be retrieved from the images acquired with this technology. Whole *in vivo* rodent brain techniques for vasculature analysis are illustrated in fig.4.1.

4.1.2 *In vivo* optical microscopy

Optical techniques represent the best strategy in order to visualize fine details in the micrometric range. With optical techniques, however, the possibility to get images deep inside organs is hindered by light scattering, so that the tissue to be exterminated must be exposed. Nonetheless, some optical technologies are able to overcome the effects of light scattering for imaging of blood vessels in animal models. Photoacustic (PA) imaging techniques use short pulses of laser irradiation to induce a transient thermoelastic expansion of biological tissues [86, 87, 88]. This expansion produces ultrasonic waves (also called PA waves), which are detected by ultrasonic transducers. The production of PA waves is directly related to optical absorption. With hemoglobin being one of the dominant absorbers in tissues, PA technology is well suited for vascular imaging. The depth achievable can approach 3 mm, with a coarse resolution when compared with traditional optical approaches (fig.4.2a).

In near-infrared II fluorescence imaging (NIR-II), light scattering is reduced thanks to the use of excitation light in the near infrared spectrum [89]. NIR-II allows fluorescence imaging beyond 2 mm through the mouse skull, with a spatial resolution of 30 μm and acquisition time of 0.2 s. Furthermore, such an acquisition speed makes real-time assessments of blood flow anomalies possible. Fig. 4.2b.

Laser speckle (LS) is another method capable of visualizing vasculature transcranially [90, 91]. LS is sensitive to the dynamic scattering of moving blood cells and can therefore be applied for the continuous imaging of blood flow dynamics. A combination of LS and dynamic fluorescent imaging, named transcranial optical vascular imaging (TOVI) can operate trough the intact skull of young mice until a depth of almost 1 mm with a spatial resolution close to 5 μm [92]. Fig.4.2c.
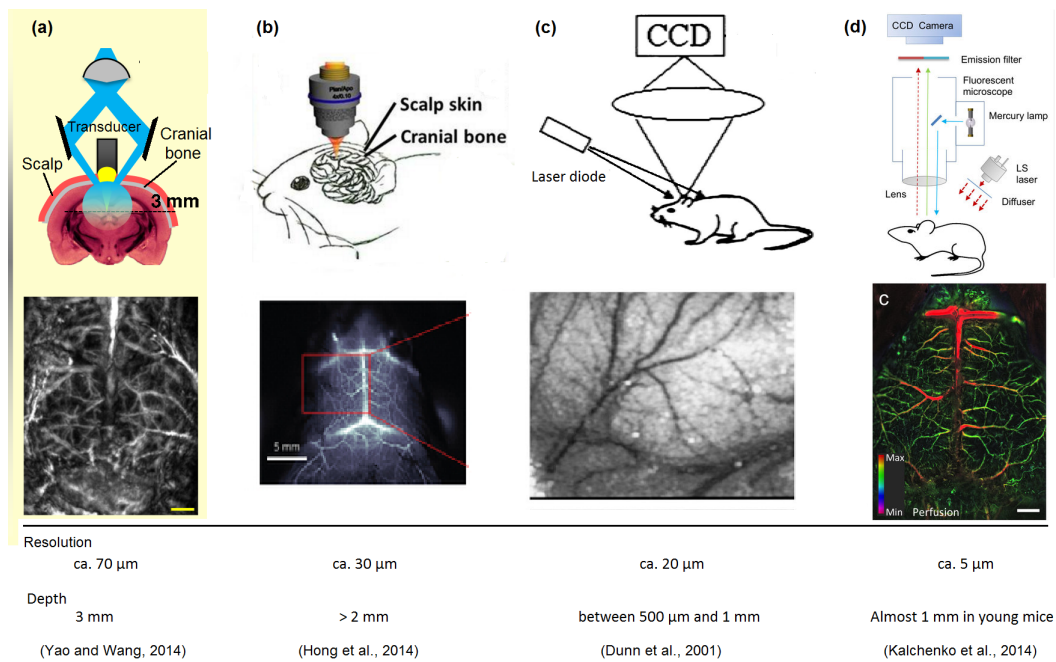
Figure 4.2: **Non invasive optical approaches** (a) Photoacustic (PA) imaging. Ultrasonic waves (yellow) are detected by an ultrasonic transducer through the intact skull of a mouse brain. Imaging depth of 3 mm can be achieved with a resolution of ~ 70 μm. (b) NIR-II. A near infrared laser is focused by an objective lens trough the mouse skull. The fluorescent emission is collected. (c) Laser speckle (LS). A laser diode beam is expanded to illuminate an area of the brain cortex. The signal is detected by a CCD camera. (d) Transcranial optical vascular imaging (TOVI). Fluorescent probes are excited by a mercury lamp, while a laser coupled with an optical diffuser is responsible for the speckle signal. Photons are detected by a CCD camera.

More invasive optical microscopy techniques are necessary to clearly distinguish the capillary network connecting large blood vessels. Two photon fluorescence microscopy (TPFM) permits image acquisitions up to a depth of about 800 μm inside tissues with subcellular resolution [61, 62]. Since light cannot pass through the skull, a cranial window is implanted to expose the brain [93]. In order to highlight the vasculature, a fluorescent marker is usually injected in the blood stream. With TPFM, changes in vascular organization at the level of the capillary network can be evaluated in mouse models of vascular impairments [94, 95]. However, the intrinsic limitations of TPFM confine the mesurements into the brain cortex. Fig.4.2d.

Small transparent animals, as larvae of zebrafish, can be studied in a non invasive manner using light-sheet fluorescence microscopy (LSFM). These animals must express fluorescent reporters to visualized the structures of interest. The fast acquisition speed of LSFM allows to follow physiological processes. For instance, live imaging of the beating zebrafish heart at a temporal resolution of more than 100 frames/cardiac cycle demonstrates the potentiality of LSFM for vascular dynamics analysis [96]. In any case, *in vivo* LSFM investigation are limited to small transparent organisms. Analysis of large samples are instead feasible *ex vivo* on fixed tissues.

4.2   *Ex vivo* brain vasculature imaging

Ex vivo methodologies are applied with the purpose of studying regions accessible only with poor resolution *in vivo*. For *ex vivo* analysis, tissues need to be treated in a way to avoid physical degradation. A classical protocol for mouse or rat tissue fixation consists of intracardial perfusion with a solution containing formaldehyde as fixative. Exploiting the vascular network, the fixative is rapidly and efficiently delivered in every area of the body. All organs or tissues are in this way preserved and can be used for imaging after excision.

In order to gain exhaustive topological informations on the vascular network, the apparatus for imaging must be able to finely detect single vessel branches and capillaries. Second, a clear distinction of blood vessels from others brain structures is necessary for automated computer analysis. In the attempt to give a clear view

on the techniques used for morphological analysis of brain vasculature, a classification into three categories is presented. These are the corrosion casting approaches, serial sectioning methodologies, and optical microscopy in combination with clearing methods.

4.2.1   Corrosion casting approaches

Vascular corrosion casts (VCCs) are replications of vessel lumen, obtained by filling the vasculature with a casting polymer. The entire vascular system of a whole animal or organ can be injected with a solidifying material, usually resins, which fills the lumen of blood vessels. The resin is allowed to cure resulting in the blood vessel network containing a solid material inside. The surrounding tissue is dissolved with corrosive chemicals, which do not affect the cured resin. VCCs obtained with this procedure can be later analyzed with different imaging techniques to study vascular morphology. One of these is scanning electron microscopy (SEM) [97, 15]. SEM is capable of producing high-resolution images of the sample surface. Very fine details can be examined, such as the shape of imprints left from endothelial cells on the vascular cast, from which it is possible to distinguish arteries from veins [98, 99]. Although tiny details are captured, imaging is limited to the surface of the cast, therefore accurate morphometric measurements are restricted to the externally visible vessels.

μCT based on conventional X-rays or synchrotron radiation (SRμCT) can be applied *ex vivo* with an increased resolution with respect to its applications *in vivo* [98, 99, 100]. Entire mouse brain VCCs have been analyzed at 16 μm resolution with μCT system [98]. A hierarchical approach combining the μCT and SEM has been proposed in order to get high resolution SEM images of regions of interested after μCT analysis (fig.4.3).

Using a fluorescent resin, also confocal light microscopy has been used to gain three-dimensional information from vascular casts, but within a limited volume. [99, 15]. Since fluorescence offers sufficient contrast with respect to the surrounding tissue, the chemical degradation step can be avoided. This opportunity permits to visualized other tissue structures specifically marked with fluorescent probes [15].
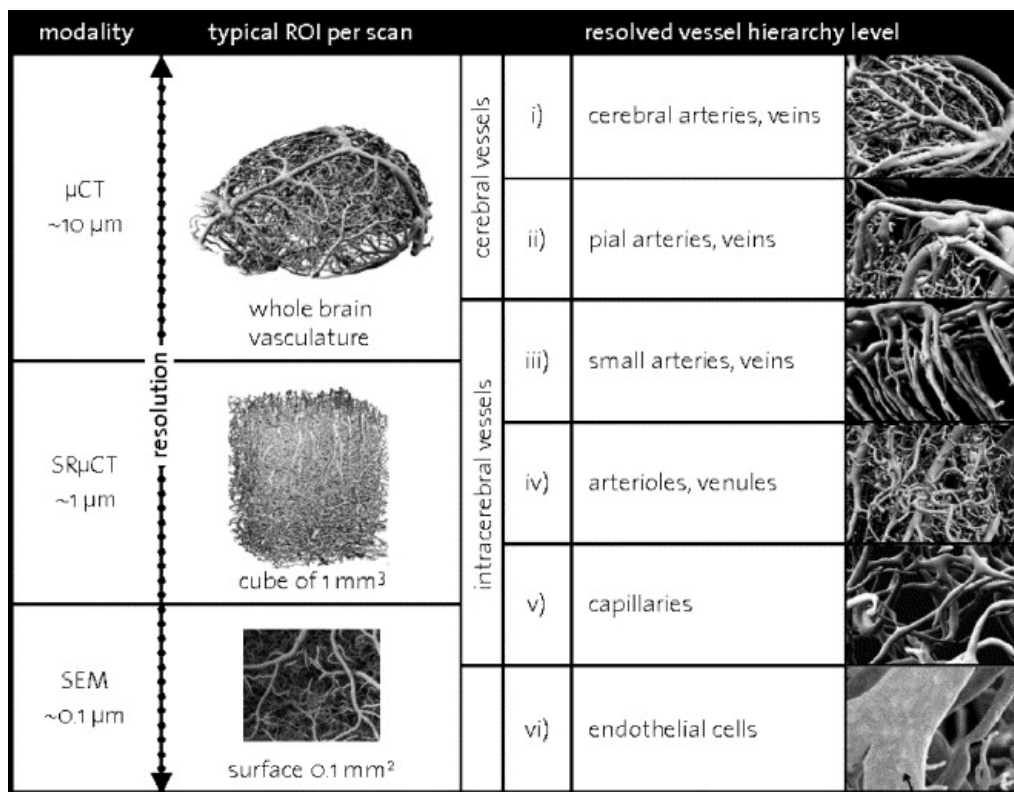
Figure 4.3: **Hierarchical approach μCT/SEM** μCT can produce a whole brain dataset from which it is possible to see large pial and cerebral arteries and veins, while small vessels are not visible. SRμCT can be used to visualized small vessels and capillaries in a confined volume. Finally SEM can unveil fine morphological structures in the nanometer range. The latter is limited to small areas. From: [98].

4.2.2 Serial sectioning methodologies

To access deep regions, serial sectioning can be applied in association with different optical techniques [8, 101, 102]. Serial sectioning approaches consist of cycles of imaging alternated with tissue sectioning for mechanical removal of the imaged volume and exposition of the underlying portion to be acquired.

By slicing the sample, serial images spaced 5μm in the z-axis, showing the vascular network, have been obtain from a mouse brain perfused with White India Ink-gelatin [101] (fig.4.4a). In this case a digital camera was adopted to acquire images of each slice surface, where vessels were visible for the white color of the

gelatin over a dark background. A volume-rendered image of the whole brain was obtained by stitching the acquired stereo images. This method, however, suffers of the presence of noise in the images, represented by white spots and straight lines not ascribable to blood vessels.

A better image quality is in principle achievable with scanning point microscopy techniques such as confocal or TPFM, the latter being the one of choice in the case of imaging in depth. However, the elevated acquisition time for image formation with scanning point methodologies makes them unsuitable for the acquisition of large volumes. Applying automatized serial sectioning, Ragan et al. demonstrated the applicability of TPFM for acquisitions of datasets of whole mouse brain expressing fluorescence in neurons [8]. This methodology, however, does not produce comprehensive information in the axial direction because of the sampling adopted, causing loss of information of 95% . The reconstruction of neuronal or vascular networks requires a finer z-sampling, which, with this methodology, would be extremely time consuming and arduous from a computational point of view since mechanical deformations occur on the cutting plane.

A fine reconstruction of neuronal nuclei and vasculature in whole mouse brain has been obtained at 1 μm voxel resolution using micro-optical sectioning tomography (MOST) [102] (fig 4.4b). Embedding the brain in hard resin, ribbons of 1μm were cut with a diamond knife and simultaneously imaged. The system consists of a reflected bright field microscope in which images are collected trough a line-scan CCD camera. The ribbons produced are free of distortions, thus alignment problems are avoided. However, the procedure is complex and a long time is required for sample preparation and imaging. Moreover, the resin embedding does not preserve fluorescence, preventing the application of differential fluorescence staining to identify structures of interest. Finally, this methodology, lacks of a specific vascular staining, relying instead on different levels of signal intensity to distinguish neurons from blood vessels in the images. A MOST technique compatible with fluorescence (fMOST) [103, 104] has been developed thanks to a novel resin-embedding method and has been used for imaging of fluorescently labeled neurons. However, no brain vasculature imaging has been reported so far with fMOST.
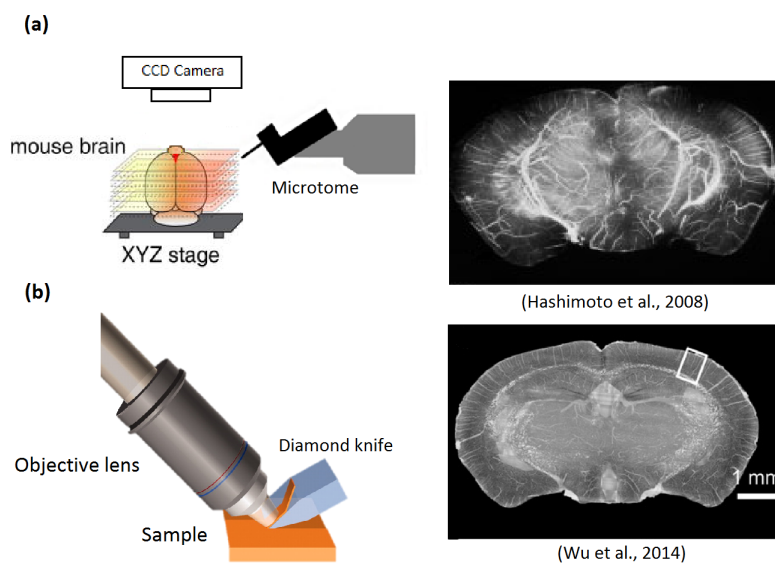
Figure 4.4: **Sectioning methodologies** (a) Serial sectioning microscopy. The brain is sliced with a microtome and images are acquired with a compound microscope equipped with a CCD camera. Vessels are visible over a dark bakground. (b) MOST. Slicing is performed by moving the specimen along the x axis to generate ribbons of about 450 mm in width and 1 μm in thickness. The ribbons are simultaneously cut and imaged using a bright-field microscope. Images are collected by the objective and recorded by a line-scan CCD. Contiguous images are stitched together using reference coordinates.

4.2.3 Optical microscopy in combination with clearing methods

Optical microscopy has been adopted to study the brain *ex vivo* in combination with a variety of approaches. Examples of optical microscopy imaging associated with vascular casting and serial sectioning have been shown above along with other imaging techniques. The introduction of novel clearing methods represented a great innovation in this field. The use of clarified samples, indeed, avoids the need of mechanical sectioning for *ex vivo* morphological analysis of a large volume, even the entire mouse brain, with optical methodologies. The advantage offered by *ex vivo* optical microscopy in terms of spatial resolution can be exploited for imaging of large specimens.

A detailed reconstruction of the vascular network, encompassing the microvasculature, has been performed on portions of mouse brain cortex with TPFM [111].

In this work a clearing agent was applied in order to enhance the depth achievable within the tissue. The vasculature was labeled with a fluorescent gel injected intracardially. Similarly to vascular casts, the gel undergoes a curing step to fill the vascular lumen. The fluorescent gel adopted is optically transparent and does not represent an obstacle along the light path. The image quality is good enough to perform vessel tracing and dissect specific features of vascular topology of the mouse brain cortex 4.5.

The main limitation of point scanning techniques, such as TFPM, lies in the long acquisition time, since the sample is scanned point by point by the laser. In LSFM, instead, the excitation light is shaped as a sheet in order to excite a plane of the sample. It relies on wide field detection, using CCD or CMOS cameras, to accurately separate photons coming from different points. Its limitation, consisting in the need of transparent samples, has been finally overcome with the introduction of clearing technologies able to make whole organs perfectly transparent. With cleared specimens, the use of LSFM can yield complete datasets of mouse brain vasculature [106, 107]. Past studies, however, anyhow, used clearing agents based on organic solvents which lead to fluorescence quenching with concomitant reduction of image quality. Moreover, the vascular staining adopted relies on endothelial markers, which only label the blood vessel wall.
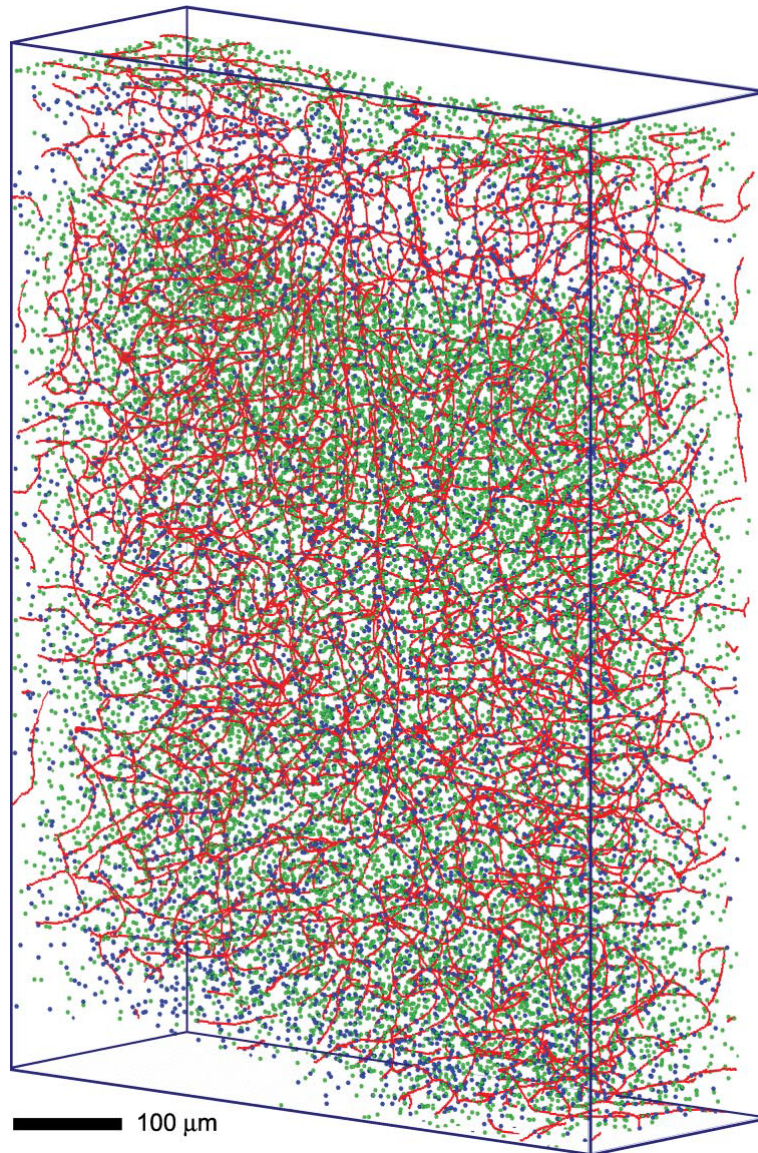
Figure 4.5: **Vascular network reconstruction with TPFM** A Volumetric reconstruction of vasculature and cell nuclei within a volume of 900x650x250 μm^3 was obtain from cortical tissue cleared with sucrose. The vasculature was stained using a gelatin conteining BSA-FITC. Cell nuclei labeled using DAPI staining. Neuronal nuclei were identify using antibodies anti-NeuN. From [111].

Chapter 5

Thesis purpose

The acquisition of full vascular datasets of whole mouse brain has been accomplished with both *in vivo* and *ex vivo* methodologies. The first suffer of poor resolution and are not suitable for dissecting the topology of the microcirculation. *Ex vivo* approaches such as LSFM in combination with clearing methods and MOST have been instead successful in acquiring complete mouse brain vascular datasets encompassing the capillary network. However, no software based vascular network reconstruction in the whole brain has been performed. In order to perform morphological analysis, the vascular network needs to be extracted by means of specific software from the dataset of images. The first step consists of successfully aligning the images in a 3D space to generate a unique file of the whole brain. Appropriate software capable of dealing with enormous amount of data has been developed for such a purpose [108]. However, the most demanding part from a computational point of view is represented by image segmentation, which means partitioning the data in an internal volume, represented by blood vessels, and a separate external volume. Various factors like non-homogeneous clearing, poor image contrast, and staining imperfections represent a serious problem in this step. The use of a labeling procedure based on fluorescent gel filling the vessel lumen, instead of the staining of endothelial wall, could be of help in this context. Subsequently, from the segmentated images, a continuous vascular network can be traced and analyzed. This last step, has been accomplished so far only in brain portions with TPFM [105] or MOST [102]. The establishment of an

efficient methodology concerning sample preparation, optical microscopy, and data management and analysis is therefore needed for an adequate morphological reconstruction of the vascular network in whole rodent brain. The high-throughput offered by LSFM could be a valid tool when used in combination with an adequate clearing procedure and staining protocol. This thesis presents a pipeline for optimal imaging of whole mouse brain vasculature with LSFM. Potential applications span from vascular characterization in healthy brain and pathological conditions, to studies devoted to a better understanding of functional imaging methodologies, used to retrieve informations about brain activity.

Part II

Methods

Chapter 6

Brain vasculature analysis

The present work aims at establishing a methodology for the analysis of the vascular component in the whole mouse brain. Various staining procedures for blood vessel staining were tested. Along with it, different approaches for tissue clearing and two optical microscopy techniques were used. In addition to wild type mice, a transgenic line expressing a fluorescent marker inside neurons was used for simultaneous or consecutive vascular and neuronal imaging. A pathological mouse model was also adopted in order to explore the potential of the staining methodology for investigations on brain vascular diseases. The mouse models and the variety of techniques for sample preparation, clearing, optical microscopy and image analysis necessary to accomplish the characterization of the procedure proposed are described in detail in the below sections.

6.1 Animal models

6.1.1 Mouse lines

Adult mice from the C57 line were used for blood vessels tomographies. For simultaneous and consecutive neuronal and blood vessels imaging, a transgenic line (Thy1-GFP-M line) of mice expressing the Green Fluorescent Protein (GFP) in sparse pyramidal neurons was used [109]. All experimental protocols involving animals were designed in accordance with the laws of the Italian Ministry of Health.

6.1.2 Surgical operations

Craniotomy was performed on an adult mouse in correspondence of the motor cortex. The mice were deeply anesthetized by intraperitoneal injection of ketamine (90 mg/kg) and xylazine (9 mg/kg). A small dose of dexamethasone (0.04 ml at 2 mg/ml) was administrated to minimize swelling at the site of surgery. A circular portion of the skull (5 mm diameter) below the motor cortex was removed and the exposed region was then covered with a coverglass and sealed with dental cement. The experimental protocols were designed in accordance with the rules of the Italian Minister of Health.

6.1.3 Photothrombotic model

The photothrombotic model was designed according to [110]. With this technique an ischemic damage is induced within a given cortical area by means of photo-activation of a previously injected light-sensitive dye. Following illumination, the dye is activated and produces singlet oxygen that damages components of endothelial cell membranes, with subsequent platelet aggregation and thrombi formation.

After anesthesia with ketamine (50 mg/kg) and xylazine (15 mg/kg), the animal was placed in a stereotaxic frame (Lab Standard^{TM} Stereotaxic Insstrument, Braintree Scientific INC) and the skull was exposed. The bregma was individuated and marked as reference point using a marker pen. Afterwards, 0.2 ml of the photosensitive dye Rose Bengal (10 mg/ml in PBS) was injected intraperitoneally. After 5 minutes, during which the dye enter the blood stream, the zone corresponding to the motor cortex was illuminated using cold light focused through an objective lens (20× ECPLAN-NEOFLUAR, Zeiss, Germany). After 15 min of illumination, the light exposure was stopped and the wound was sutured. Mouse perfusion and labeling was performed one month after stroke induction.

6.2 Blood vessel staining

6.2.1 Hydrogel-BSA-FITC staining

Seeking for a CLARITY compatible blood vessel lumen staining, a step was added to the CLARITY perfusion protocol described in [80]. Briefly, after perfusion with 20 ml of 0.01M of phosphate buffer saline (PBS) solution (pH 7.6), the mouse was perfused with 10 ml of Hydrogel solution, followed by 20 ml of Hydrogel in which fluorescein (FITC)-conjugated albumin (no. A9771; Sigma) 1% (w/v) was dissolved.

6.2.2 Gel-BSA staining

For blood vessel lumen staining the protocol described in Tsai et al., 2009 [111] was used. After deep anesthesia with isoflurane inhalation, the mice were transcardially perfused first with 20-30 ml of 0.01M of phosphate buffered saline (PBS) solution (pH 7.6) and then with 60 ml of 4% (w/v) paraformaldehyde (PFA) in PBS. This was followed by perfusion with 10 ml of a fluorescent gel perfusate, with the body of the mouse tilted by 30°, head down, to ensure that the large surface vessels remained filled with the gel perfusate. The body of the mouse was submerged in ice water, with the heart clamped, to rapidly cool and solidify the gel as the final portion of the gel perfusate was pushed through. The brain was carefully extracted to avoid damage to pial vessels after 30 min of cooling and incubated overnight in 4% PFA in PBS at 4°C. The day after the brain was rinsed 3 times in PBS.

6.2.3 Lectin staining

For blood vessel wall staining the mouse was anesthetized with isoflurane and manually perfused with 15 ml of ice cold PBS 0.01M . The mouse was tilted by 30° head down and perfused with 10 ml of ice cold PBS containing 0.1mg/ml lectin-FITC from *Lycopersicon esculentum* (Sigma-Aldrich, L0401). After 7 min of incubation, during which lectins were allowed to firmly bind the vessel wall, 40 ml of 4% PFA in PBS was injected. The brain was extracted and incubated

overnight in 4% PFA in PBS at 4°C. After incubation the brain was rinsed 3 times in PBS.

6.2.4   Gel compositions

Gel solutions were made of porcine skin gelatin type A (no. G1890; Sigma) in which fluorescein (FITC)-conjugated albumin (no. A9771; Sigma) or Tetramethyl-rhodamine (TRITC)-conjugate albumin (Thermo Fisher Scientific A23016) were dissolved. A 2% (w/v) solution of gelatin is prepared in boiling PBS and allowed to cool to <50°C. It was then combined with 1%(w/v) albumin-FITC (BSA-FITC), or 0.05% albumin-TRITC (BSA-TRITC). The solution was maintained at 40°C with stirring before perfusion.

6.2.5   *In vivo* staining

An adult mouse was anesthetized with an intraperitoneal injection of ketamine (50 mg/kg) and xilazine (9 mg/kg). After placing the mouse in a stereotaxic platform for head fixation, 0.2 ml of a solution of Texas red-destran (140 μg/ml) in saline solution was injected into the tail vein.

6.2.6   Differential stainings of arteries and veins

For differential staining using gel and antibody anti-veins endothelium, the mouse was anesthetized by isoflurane inhalation and transcardially perfusion with 20 ml of ice cold PBS. 200 μg of anti-endomucin FITC conjugated (sc-65495 FITC Santacruz Biotechnologies) in 10 ml of ice cold PBS were then injected with the mouse tilted 30° head down. After 7 minutes, to allow stable antibody binding to the endothelium surface, 40 ml of ice cold PFA 4% in PBS solution was injected. Subsequently, the injected solution was switched to 10 ml of BSA-TRITC gelatin. The body of the mouse was submerged in ice water, with the heart clamped, for 30 min. The brain was carefully extracted and incubated overnight in 4% PFA in PBS at 4°C. The day after the brain was rinsed 3 times in PBS.

For differential staining using BSA-FITC and BSA-TRITC gels, the mouse was first anesthetized by isoflurane inhalation and transcardially perfused with 30 ml

of PBS at room temperature. Subsequently, 50 ml of PFA 4% in PBS solution at room temperature was injected. Afterwards, 10 ml of Gel-BSA-TRITC followed by 0.2 ml of Gel-BSA-FITC were injected with the mouse tilted 30° head down. The body of the mouse was submerged in ice water, with the heart clamped, for 30 min. The brain was carefully extracted and incubated overnight in 4% PFA in PBS at 4°C. The day after the brain was rinsed 3 times in PBS.

6.3   Evaluation of the staining methodology

6.3.1   Morphological changes assessment

After *in vivo* vasculature staining, imaging was performed with a custom-made TPFM . Automatic acquisitions of adjacent regions were taken with 50 μm overlap between adjacent stacks, using a custom software written in LabView (National Instruments, TX). After *in vivo* imaging, the mouse was perfused for blood vessel staining with Gel-BSA-FITC. Using big vessels as reference, *ex vivo* imaging of the same brain area was performed with TPFM.

Comparison of vessel size diameter between *in vivo* and *ex vivo* imaging was performed with ImageJ software. Blood vessel length was measured by manual tracing of selected vessels with the Filament Editor of Amira software.

6.4   Signal to background ratio measurements

Images of lectin-FITC and Gel-BSA-FITC samples cleared with TDE 47% were acquired with TPFM. The signal to background ratio was calculated from the images every 20 μm over a depth of 500 μm. The mean grey value of selected ROIs in correspondence with vessels signal or sourrounding background was used for the measurements. Six stacks for each sample were used.

6.5   Segmentation assessment with TPFM

From the images acquired with TPFM, manual segmentations of Lectin-FITC and Gel-BSA-FITC stained samples were performed. These were compared

with automatic segmentation by superimposition of MIPs corresponding to the same regions. A colocalization tool of ImageJ (JACoP plugin) was applied to retrieve the overlap coefficient as percentage value, indicated in the graph as "true positive", and the percentage of non overlapping regions of the automatically segmented stack (false positive) and the percentage of non overlapping regions of the manually segmentated stack (false negative).

6.6 Imaging modalities

6.6.1 Two-photon microscopy imaging

A custom-made two-photon fluorescence microscope (TPFM) was constituted by a mode locked Ti:Sapphire laser (Chameleon, 120 fs pulse width, 80 MHz repetition rate, Coherent, CA) coupled into a custom-made scanning system based on a pair of galvanometric mirrors (VM500+, Cambridge Technologies, MA). The laser was focused into the specimen by a water immersion $20\times$ objective lens (XLUM 20, NA 0.95, WD 2mm, Olympus, Japan) for uncleared speciments and *in vivo* mesurements. A tunable $25\times$ objective lens (LD LCI Plan-Apochromat, NA 0.8, WD 0.55mm, Imm Corr DIC M27, Zeiss, Germany) was used for correlative experiment. A tunable $25\times$ objective lens (Glyc MP FN18, NA 1.00, Olympus, Japan) was instead used for stroke analysis. For Gel-BSA-FITC and lectin-FITC stained samples cleared with 47%TDE/PBS (RI 1.42), a tunable $20\times$ objective lens (Sca*le* LD SC Plan-Apochromat, NA 1, WD 5.6mm, Zeiss, Germany) was used.

The system was equipped with a motorized xy stage (MPC-200, Sutter Instrumente, CA) for lateral displacement of the sample and with a closed-loop piezoelectric stage (ND72Z2LAQ PIFOC objective scanning system, 2mm travel range, Physik Instrumente, Germany) for the displacement of the objective along the z axis. The fluorescent light is separated from the laser optical path by a dichroic beam splitter (DM1) positioned as close as possible to the objective lens (non-de-scanning mode). A two-photon fluorescence cut-off filter (720 SP) eliminates reflected laser light. A second dichroic mirror (DM2) is used to split the two spectral components of the fluorescence signal. The fluorescence signals are

filtered with 630/69 and 510/42 filters (FF1 and FF2) and collected by two orthogonal photomultiplier modules (H7422P, Hamamatsu Photonics, Japan). The instrument was controlled by custom software, written in LabView (National Instruments, TX).

6.6.2   Light-sheet microscopy imaging

Whole brains were imaged using a custom-made light-sheet microscope described in [112]. The light sheet is generated using a laser beam scanned by a galvanometric mirror (6220H, Cambridge Technology, MA); confocality was achieved by synchronizing the galvo scanner with the line read-out of the sCMOS camera (Orca Flash4.0, Hamamatsu Photonics, Japan). The laser light was provided by a diode laser (Excelsior 488, Spectra Physics) and an acoustooptic tunable filter (AOTFnC- 400.650-TN, AA Opto-Electronic, France) was used to regulate laser power. Excitation was λ= 561nm for TRITC and λ=491nm for GFP and fluorescein. The excitation objective was 10X, 0.3 NA Plan Fluor from Nikon, while the detection was 10X, 0.6 NA Plan Apochromat from Olympus. This latter has a correction collar for the refractive index of the immersion solution, ranging from 1.33 to 1.52.

The samples were place in a quartz cuvette containing the mounting medium 63% TDE/PBS and placed in a custom made chamber filled with the mounting medium. The samples were mounted on a motorized x-, y-, z-, θ-stage (M-122.2DD and M-116.DG, Physik Instrumente, Germany) which allowed free 3D motion and rotation. The microscope was controlled via custom written LabVIEW code (National Instruments) which coordinated the galvo scanners, the rolling shutter and the stack acquisition.

Although in principle with LSFM it is possible to generate a light sheet wide enough to illuminate an entire mouse brain section, some constraints limit the width of the light sheet. The wider is the laser width, the lower is the laser power at any point of the illuminated volume. This eventually results in a less efficient fluorescence excitation. A second limiting factor is the width of the digital camera used for acquisitions. To keep an high image resolution, larger imaged areas must be focus on larger cameras with the same pixel density. This lead to a remarkable

price increase of the apparatus. The setup used for this thesis is provided with a sCMOS camera of 1.3 mm². In order to reconstruct the entire volume, regions of superimposition were present among the acquired stacks. Ultimately, a specific software was used for volumetric reconstruction (see 6.8.1).

6.7 Samples clearing procedures

6.7.1 TDE clearing

For two-photon imaging, fixed brain slices labeled with gel BSA-FITC or Lectin-FITC were cleared with serial incubations in 20 ml of 20% and 47% (vol/vol) 2,2'-thiodiethanol in 0.01M PBS (TDE/PBS), each for 1 hour at 37°C in gentle oscillation.

Dissected mouse brain cortex were cleared with two serial incubation in TDE 30% for 1h at room temperature (RT) and TDE 63% for 3h (RT) while rotating. After clearing they were ready for imaging.

6.7.2 CLARITY-TDE clearing of whole mouse brain

Fixed mouse brains were incubated in Hydrogel solution (4% (wt/vol) PFA, 4% (wt/vol) acrylamide, 0.25% (wt/vol) VA044) in 0.01M PBS at 4°C for 1 week following the protocol described in [80] for fixed tissues. Samples were degassed and incubated at 37°C for 3 hours to allow hydrogel polymerization. Subsequently, the brains were extracted from the polymerized gel and incubated in clearing solution (sodium borate buffer 200 mM, 4% (wt/vol) Sodium dodecyl sulfate) (pH 8.5) at 37°C for one month while gently shaking. The samples were then washed with PBST (0.1% TritonX in 1X PBS) twice for 24 hours each at room temperature. Mouse brain samples treated with CLARITY were optically cleared with serial incubations in 50 ml of 30% and 63% (vol/vol) 2,2'-thiodiethanol in 0.01M PBS (TDE/PBS), each for 1 day at 37°C while gently shaking before imaging with light-sheet microscope as described in [9].

6.8 Image processing and data analysis

6.8.1 Image stitching and 3D rendering

LSFM produced a series of 3D stacks with regions of superimpositions. To achieve a 3D image of whole specimens from raw data the Terastitcher tool[108], a sofware capable of dealing with teravovel-sized images, was used.

Graphs and data analysis were done with OriginPro 9.0 (OriginLab Corporation). Image stacks were analyzed using both Fiji (http://fiji.sc/Fiji) and Amira 5.3 (Visage Imaging) software. 3D renderings of stitched images were produced from downsampled files using the Amira Voltex function. The Filament Editor of Amira was used to manually trace vessels segments.

6.8.2 Image segmentation

For segmentation of two-photon images, a segmentation algorithm based on Markov random field described in [113] was used. The segmentation of a transverse section from the stitched data of the whole brain dataset, acquired with LSFM, was obtain by simple thresholding with imageJ.

6.9 Brain cortex vasculature analysis with TPFM

6.9.1 blood vessels orientation and density analysis

Mice were perfused with the protocol described for vessel staining (see 6.2.2). The cortex was subsequently dissected from the fixed brain under a stereomicroscope. The dissected cortex were cleared with TDE 63% and flattened with a quartz coverslip. Region of 1x2 mm caudally from the stroke and 700 μm depth were imaged with a z-step of 3μm. For each sample MIPs of 160 μm were taken, under the surface in order to avoid big vessels. Four MIPs of proximal regions (within 500 μm from stroke), and four MIPs of distal regions (between 1 and 1.5 mm from stroke) for each mouse were used for analysis of vessels orientation. The imagej plugin orientationj was used for orientation profile measurements.

For vessels density analysis the stacks were first binarized using an automatic thresholding with ImageJ. The sum of the pixel count from the histogram was used as measure of blood vessel density, starting 100 μm under the surface in order to avoid large superficial vessels.

Part III

Results

Chapter 7

Validation of vessel staining methods

Vascular staining relying on lectin binding to sugar complexes on endothelial walls has been applied in combination with clearing methods based on organic solvents [106] or tissue transformation [115]. The high transparency achieved with these clearing methods allows whole mouse brain imaging without mechanical sectioning. However, the lack of staining in the vessel lumen makes the development of software-based methodologies for vascular network reconstruction arduous. Among the clearing methods proposed in literature, tissue transformation, i.e. CLARITY, offers an improved fluorescent preservation with respect to organic solvents, and was chosen in this thesis as preferential clearing procedure for whole mouse brain imaging. In search for a vascular staining able to fill blood vessels, and compatible with CLARITY, two different approaches have been tested. The one resulting in optimal outcome has been compared with lectin staining for automated image segmentation.

7.1 CLARITY compatible blood vessels lumen staining

In CLARITY, tissue transparency is obtained by selective removal of lipids. Proteins are instead retained thanks to functional groups binding acrylamide and

PFA monomers. Hence, a protein-conjugated fluorophore was used for labeling, specifically, albumin-FITC conjugate (BSA-FITC). The high molecular weight of albumin ensures that the marker is retained inside blood vessels, indeed serum proteins such as BSA cannot cross the blood vessels wall.

In CLARITY, a solution of hydrogel is used during mouse perfusion in place of PFA. For vessel labeling, a perfusion step was added to the CLARITY perfusion protocol, in which a solution of hygrogel containing BSA-FITC was injected. It was then determined whether cross-links between hydrogel monomers and BSA-FITC allowed the marker to completely fill the blood vessels lumen. Unfortunately, the staining did not result homogeneous. In particular big holes were present in large blood vessels (fig. 7.1a) and void spaces could also be detected in capillaries (fig. 7.1b). Lots of trials were done in the pursuit to solve the problem: changes in the concentration of hydrogel components, tilting of the mouse during perfusion, degassing of solutions before perfusion, variations on time and temperature of the polymerization step, changes on the time of degassing step and the use of high power vacuum pump. In any case none of the protocol changes improved the labeling.

A protocol described in Tsai et al. [111], which uses a fluorescent solution composed of BSA-FITC dissolved in porcine skin gelatin, has shown to be effective for blood vessel lumen staining. Both the fluorescent marker and the gel are made of proteins, so they are in principle able to be retained in the hydrogel matrix during the aggressive washing out of the lipid component. However, the intracardiac injection of this gelatin is incompatible with hydrogel perfusion because of the different temperatures of polimerization of hydrogel and gelatin.

Even so, a passive diffusion of acrylamide monomers and PFA throughout the tissue can be achieved by simple incubation of fixed samples in hydrogel solution for some days. The staining procedure of Tsai et al. (hereafter Gel-BSA-FITC) was then used in combination with CLARITY protocol for fixed samples. In this case the marker appeared homogeneously distributed both inside pial vessels (fig. 7.1c) and capillary network (fig. 7.1d). It is supposed that the protein component of the gel is retained inside blood vessels, promoting the creation of an homogeneous network inside vessel lumen upon polymerization. The capability of hydrogel monomers to cross the vessels wall, instead, would not allow a dense and

even distribution inside blood vessels, creating void spaces.

Transgenic lines expressing a fluorescent marker inside neurons are extensively used in research. A vascular detection based on fluorescence, enables related studies of fluorescently labeled neurons and vascular component. In order to avoid fluorescence overlap, the fluorescence emission spectra associated with blood vessels can be changed using a different BSA conjugated fluorophore. To simultaneously visualize vessels and neurons in Thy-1 GFP-M mouse, BSA-FITC was replaced with BSA-tetramethylrhodamine (BSA-TRITC) (Fig. 7.2).

7.2   Gel staining vs lectin staining

The advantage of Gel-BSA-FITC staining over lectin-FITC consists of the capability to fill the lumen of blood vessels (fig. 7.3). As a first consequence, a greater fluorescent signal is detected, as evaluated in terms of signal to background ratio over depth (fig. 7.3e). Averaging the signal detected at any depth, it results in ten fold increase in signal/background using the gel (fig. 7.3f). The 3D representation shown in fig. 7.4 gives an idea about differences of the signal detected along depth.

The better signal to background ratio offers an easier demarcation of blood vessels, which is relevant for partitioning the image in an internal volume, consisting of blood vessels, and an external volume. This process is called image segmentation and represent a crucial step for subsequent morphological analysis. Because of the amount of data, image segmentation must be automatized with specific softwares. The presence of fluorescence only in the vessels wall using lectins is not a trivial detail, since the volume inside blood vessels, detected as void space, must be discerned from the external void by the segmentation algorithm. Such a computational step is instead completely avoided with the use of gels filling the vessels lumen. The results of automatic segmentation for Lectin-FITC and and Gel-BSA-FITC staining are shown in fig. 7.5. Because of the low signal with Lectin-FITC staining, no blood vessels are detected after few hundred microns. To evaluate the accuracy of automatic segmentation, it has been superimposed with a manual segmentation of the same maximum intensity projections (MIPs) and the percentages of shared pixels (true positive) as well as the percentage of

Lectin-FITC   **Gel-BSA-FITC**
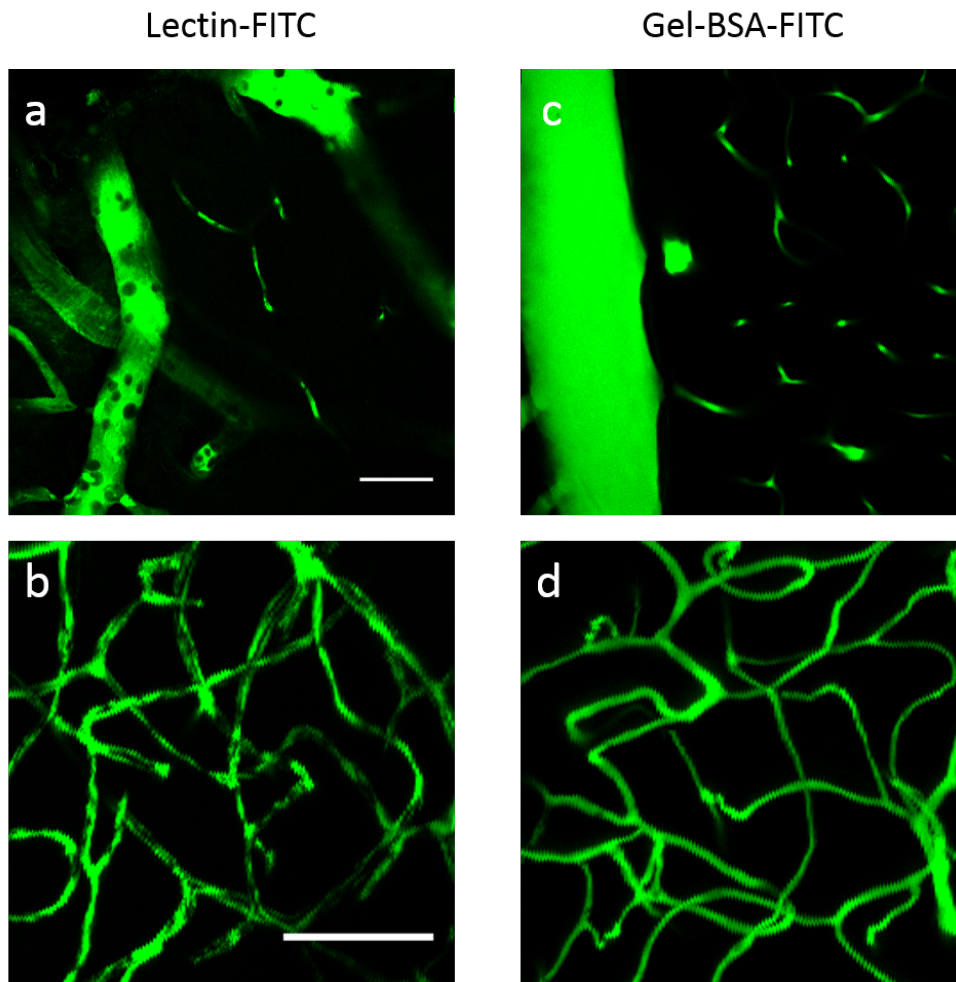
Figure 7.1: **Vessel staining** (a, b) The direct injection of the marker concurrently with hydrogel perfusion did not result in optimal vessel staining, neither for large pial vessels (a) or capillaries (b). Vessel staining using gelatin mixed with BSA-FITC demonstrated instead to be effective for homogeneous marker distribution (c, d). Images acquired with TPFM. Scale bar=500 μm.
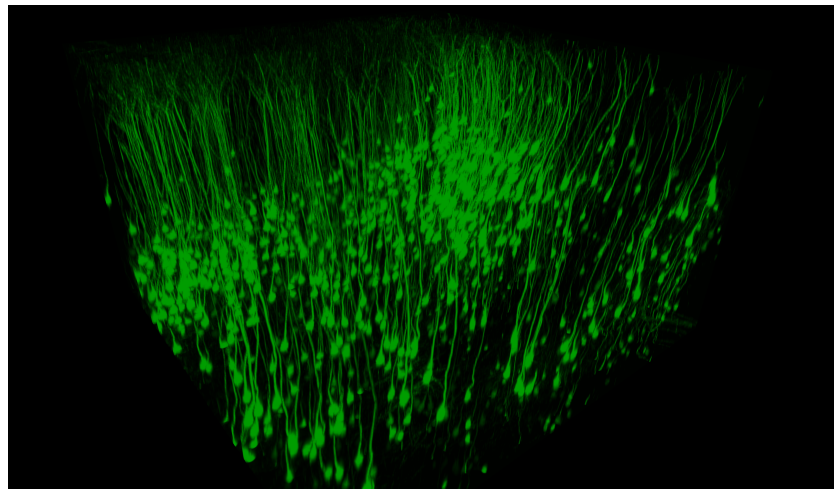
(a) Neurons (GFP)
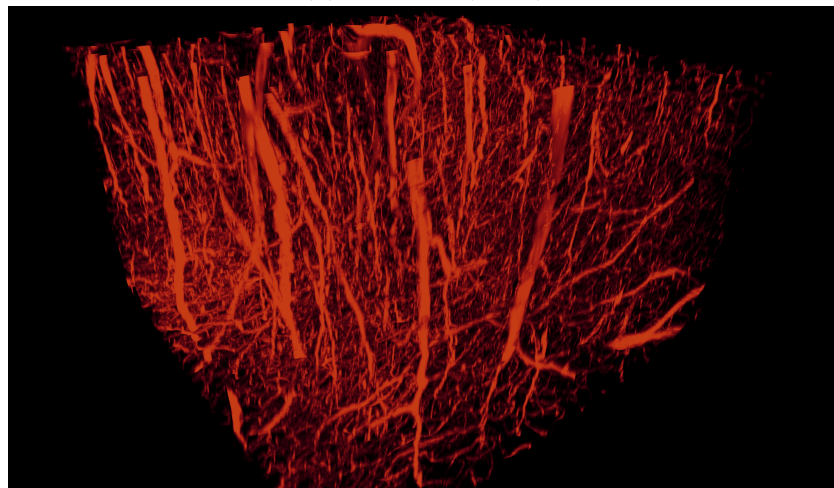
(b) Vessels (TRITC)
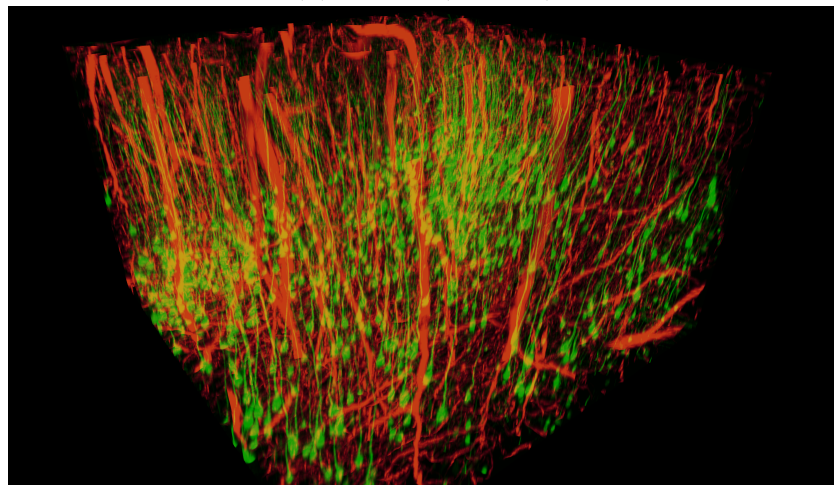
(c) Merge

Figure 7.2: **Simultaneous neuron and vessel imaging** GFP expressing neurons and blood vessels can be simultaneously visualized replacing BSA-FITC conjugate with gel BSA-TRITC conjugate in the gel composition. Images were acuired with TPFM and stack were stitched in 3D dimensions using the Terastiching software [108]. 3D rendering with Amira software. Images dimension 1x1x0.7 mm.
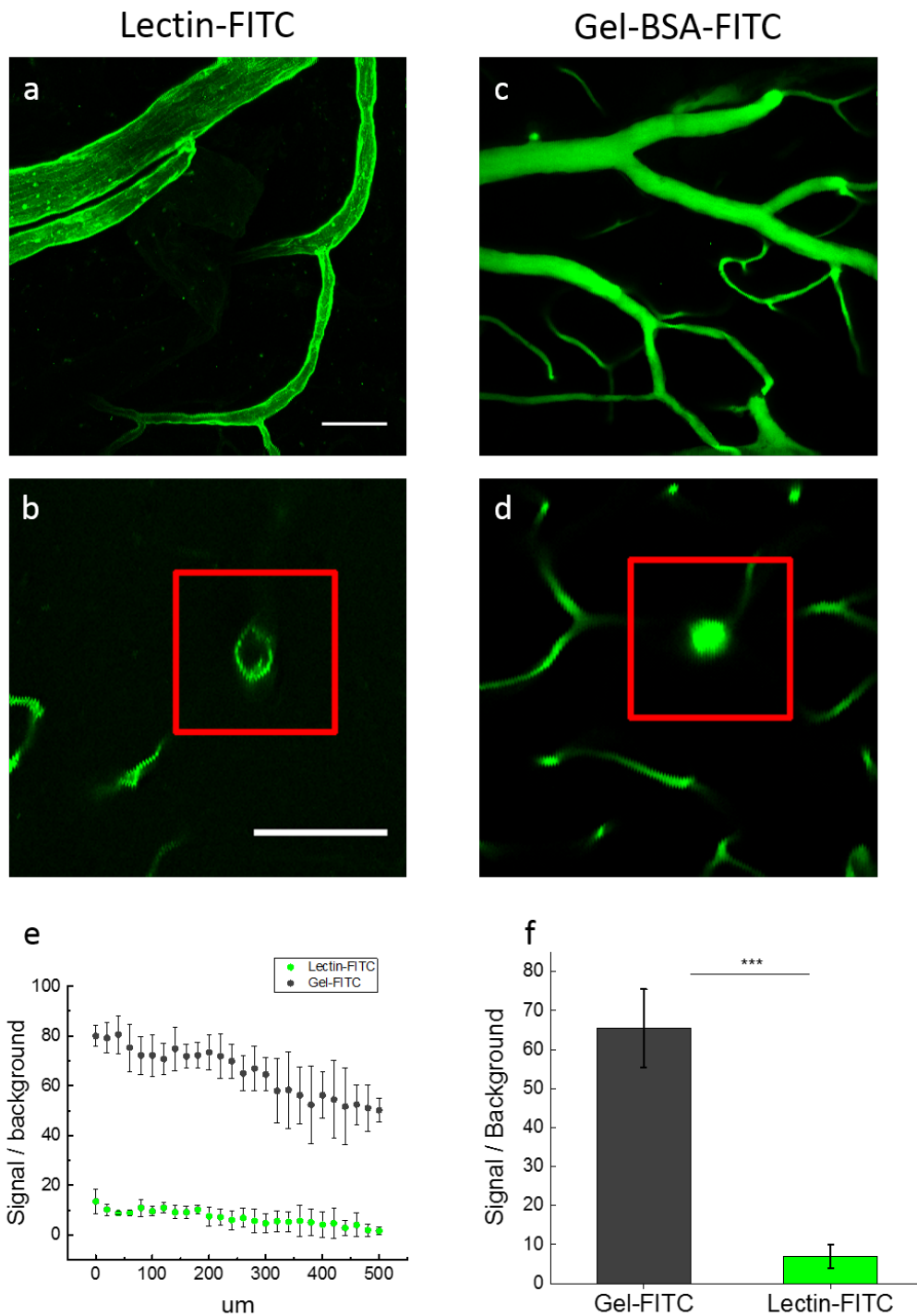
Figure 7.3: **Comparison between Lectin-FITC and Gel-BSA-FITC staining** Fluorescence is absent inside blood vessel lumen in Lectin stained samples (a,b). Gel-BSA-FITC staining completely fills the lumen inside blood vessels (c,d). Red Insets on vessels arranged perpendicularly to the plane of imaging. Scale bars=50 μm. Images acquired with TPFM. (e,f) Graphs showing signal over background ratio along depth (e) and on average (f). n=6.
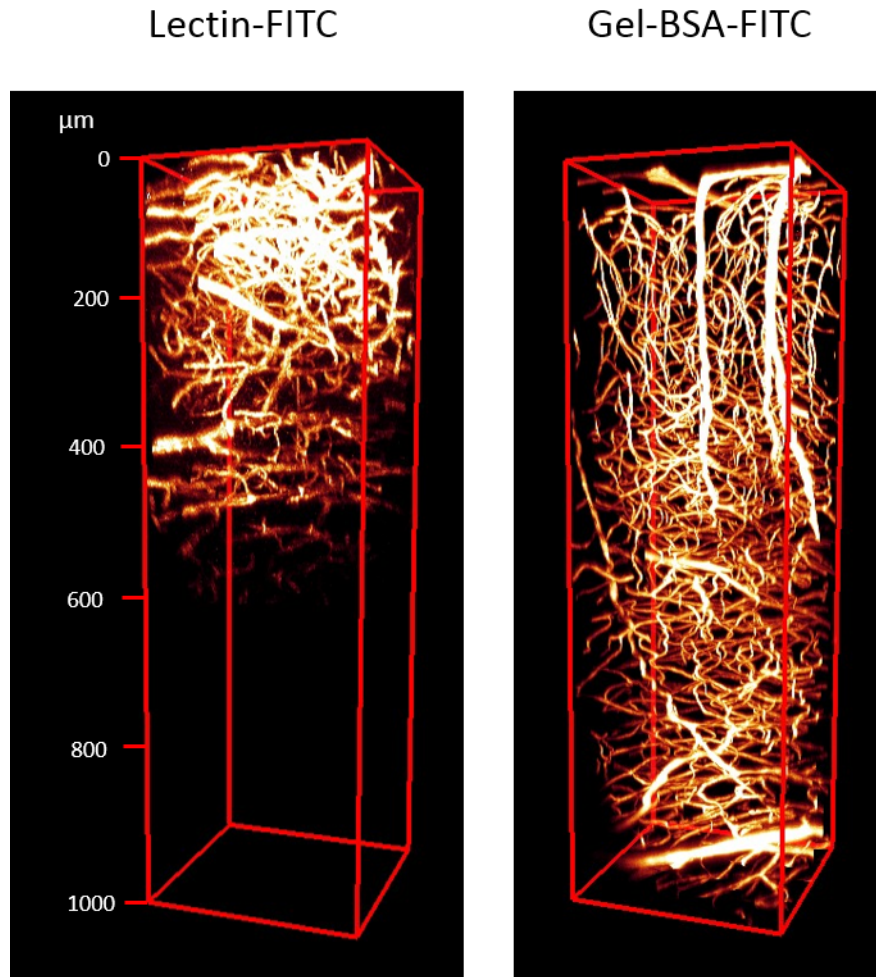
Figure 7.4: **Comparinson between 3D rendered images** Images showing differences in the signal detected along depth between Lectin-FITC and Gel-BSA-FITC stained samples. The rapid decrease of the signal detected in the Lectin-FITC labeled sample causes a substantial worsening in image quality after a few hundred microns. In Gel-BSA-FITC stained sample, image quality was preserved along the depth of the stack. The samples were cleared with TDE 47% before imaging to increased the depth achievable. Images acquired with TPFM and 3D rendered with Amira. Image dimension 0.3x0.3x1 mm.
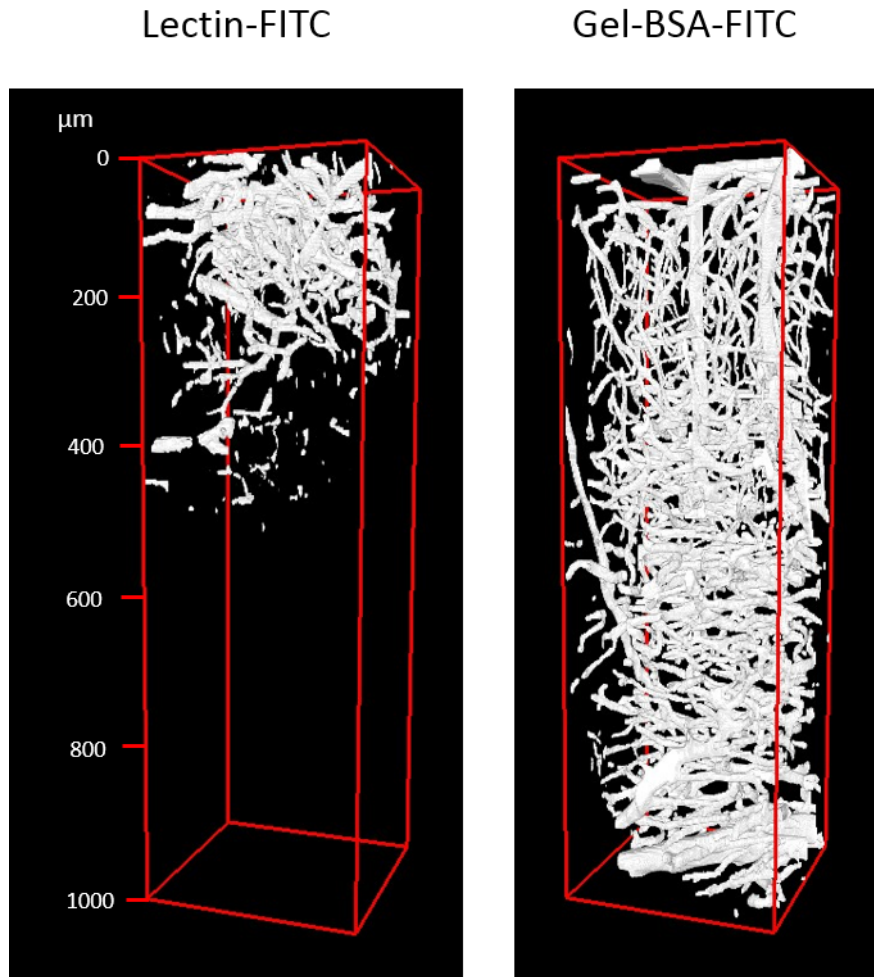
Figure 7.5: **Image segmentation** A comparison between segmented lectin-FITC and Gel-BSA-FITC stacks is shown. The better image contrast of gel staining allowed for a proper segmentation in deep regions. 3D renderings of the segmented stacks were obtained with Amira software. Image dimension 0.3x0.3x1 mm.

pixels detected only by automatic segmentation (false positive) or only by manual segmentation (false negative) have been quantified over a depth of 240 μm, after which the poor image contrast of Lectin-FITC staining did not allow for a clear blood vessel distinction (fig. 7.6). While with Gel-BSA-FITC staining the overlap coefficient remained stable over depth to a value higher than 90%, with Lectin-FITC was observed a rapid drop from 0.84% to 0.44% at a depth of 200 μm. False positive are due to an oversegmentation of the algorithm with respect to the manual segmentation. The false positive values remained stable over depth for both methods, being however lower with Gel-BSA-FITC (ca. 0.1% against 0.16%). Becouse of the poor signal, the false negative increased considerably with Lectin-FITC stain, from 0.16% within 100 μm in depth to 0.77% after 200 μm. Using Gel-BSA-FITC staining a small increase from 0.05% to 0.08% was observed.

7.3 Evaluation of morphological changes with respect to *in vivo*

Possible morphological alterations due to the staining procedure, could yield misleading topological results, not consistent with the real morphology. To verify the accuracy of the data produced, a comparison between *in vivo* and *ex vivo* imaging has been carried out (fig 7.7). For *in vivo* TPFM, craniotomy was performed in order to expose a region of the mouse brain.

After staining, changes in blood vessels diameter were visible. While some vessels enlarged their diameter, others reduced their size. Red and yellow insets in fig. 7.7b highlight respectively an enlarged and a shrunk vessel with respect to *in vivo* imaging (fig. 7.7a). Plotting the vessel diameter size calculated from *in vivo* and *ex vivo* images, the fitting curve shows a slope towards the *ex vivo* axes, indicating a general increase in vessel diameter (fig. 7.7c). Nonetheless, the majority of the capillary segments analyzed is above the fitting curve, suggesting a different trend for small vessels. The differences in vessel diameter between *ex vivo* and *in vivo* could be ascribed to altered flow rates during perfusion along with the effects of fixative solutions. However it has to be taken in consideration that in living animals cerebral blood regulation implicates differential perfusion of
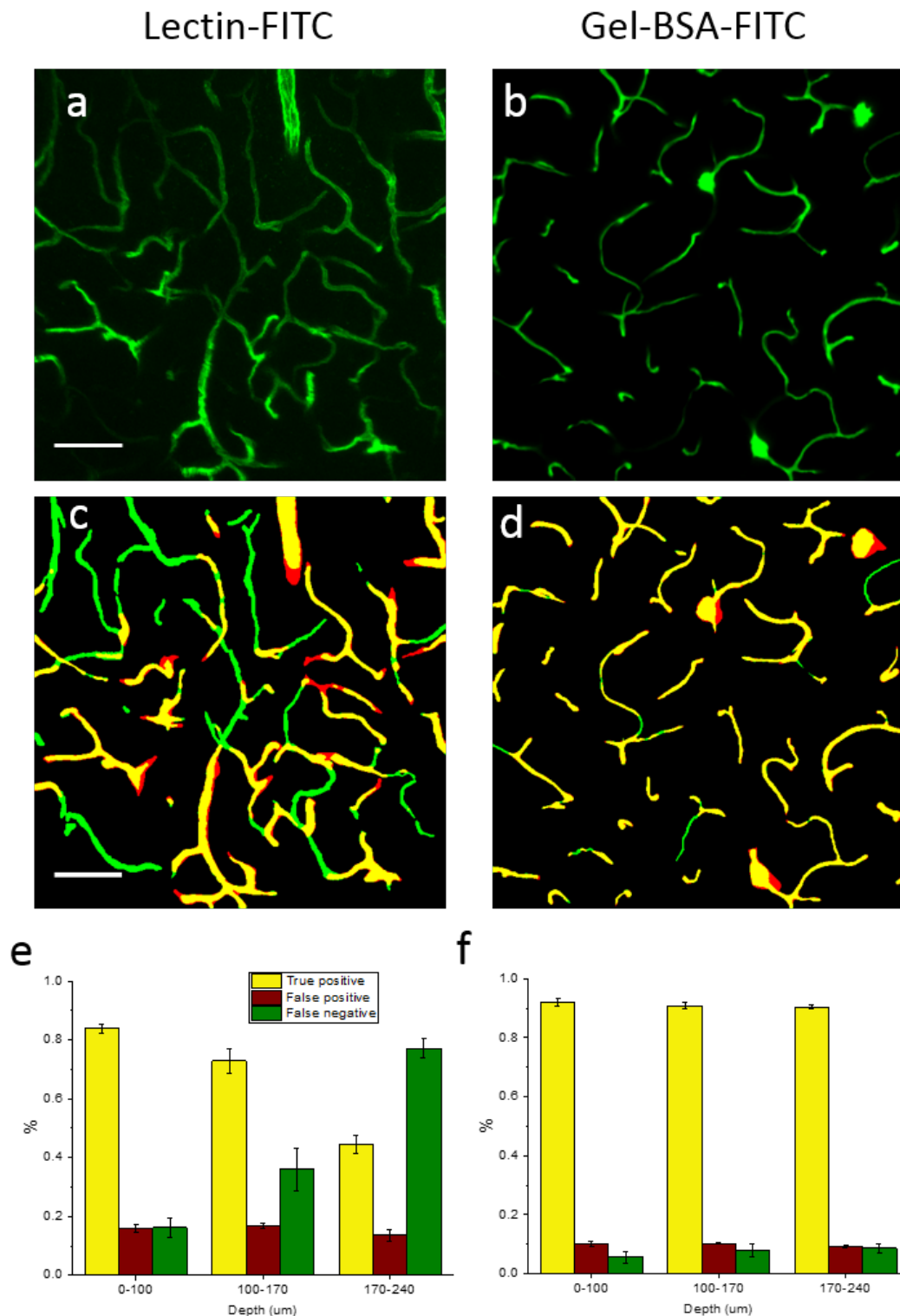
Figure 7.6: **Evaluation of automatic segmentation** (a, b) MIPs from original stacks of Lectin stained (a) and Gel-BSA-FITC stained (b) vasculature, 110 μm under the surface. (c, d) Superimpositions of MIPs from automated and manually segmented stacks. Regions of superimposition are represented in yellow. Green and red color correspond to manual and automatic segmentation respectively. Scale bar=50 μm. (e, f) Overlap coefficient (yellow bars), and the false positive (red) and false negative (green) percentage at different depths.

brain areas based on cerebral activity. This mechanism, known as neurovascular coupling, determines changes in blood flow and vessels intraluminar diameter *in vivo* [12].

A map of the vascular network, can however be traced independently from vessel diameter. To evaluate the possibility to perform accurate vascular tracing, the length of vessel segments, measured in 3D modality, was compared (fig. 7.7d). In this case, the slope of the fitting curve was close to 1, revealing an overall maintaining of vessel length. Moreover, a great correlation value was found (R=0.999), indicating a good preservation at the level of single vessels, and not only a main trend. From these measurements it can be inferred that a map of the vascular network can be reliably extracted.

7.4   Distinction between arteries and veins

From both a structural and a functional point of view, blood vessels can be distinguished in arteries and veins, interconnected by a bed of capillaries. With the pursuit to obtain a differential staining of the two sets, two different approaches were tried. The first one is based on the use of a fluorophore-conjugated antibody (anti-endomucin-FITC) capable of binding to a specific component of the venular endothelium (fig 7.8 left). Venous endothelium labeling with anti-endomucin-FITC was added to the lumen staining protocol with Gel-BSA-TRITC. As a consequence, only the venular endothelium was labeled with the antibody (green fluorescence), while the lumen of both arteries and veins was instead labeled with Gel-BSA-TRITC (red fluorescence).

The second approach is based on the use of two gels containing two different fluorophores, which are BSA-FITC and BSA-TRITC. The procedure consists in a first intracardial perfusion with Gel-BSA-TRITC, after which the whole vasculature is uniformly labeled. In a second step, a minimal quantity of Gel-BSA-FITC (0.2 ml) is used for perfusion. While the Gel-BSA-TRITC is forced out from arteries towards veins, the quantity of Gel-BSA-FITC injected is not enough to exit veins. The consequence of this is a differential staining of arterial and venous vascular lumen.

While the first approach relies on a specific vein staining, the second one is
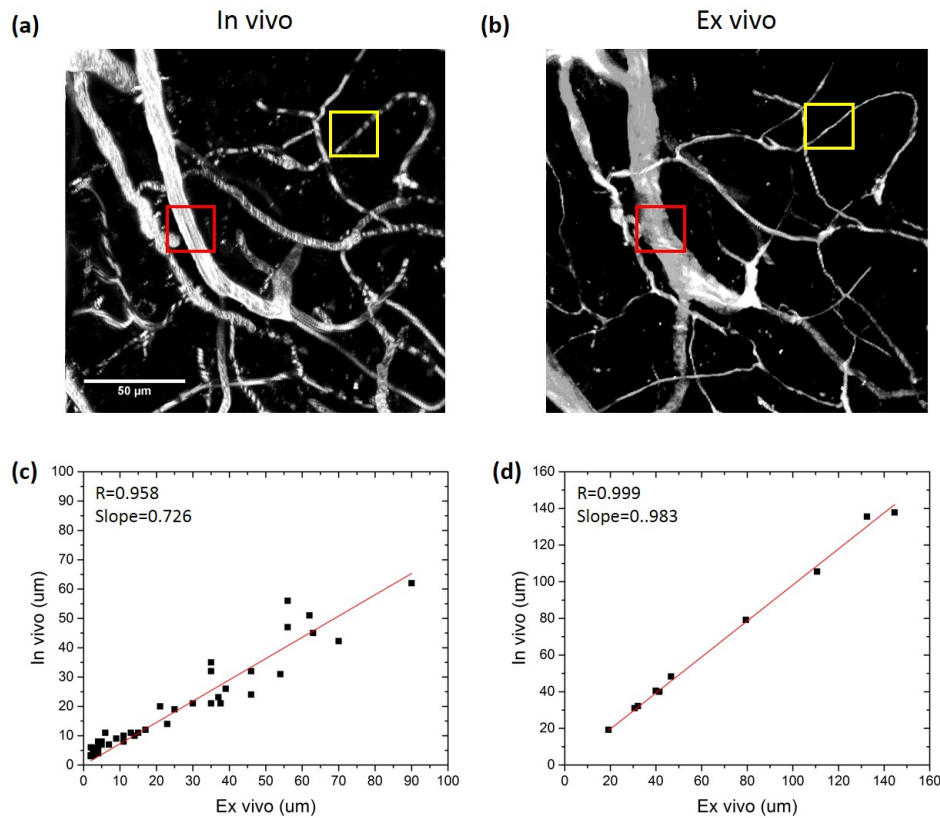
Figure 7.7: **Evaluation of morphological changes** (a,b) Comparison between *in vivo* and *ex vivo* vascular staining. For a visual comparison, stacks were rotated using Amira software to obtain the same orientation. Red and yellow insets showing respectively enlarged and shrunk vessels upon *ex vivo* staining. (c) Comparison of vessel dimension between *in vivo* and *ex vivo*. While part of the vessels retain the same size, others show a major or minor size with respect to *in vivo* imaging. The slope of the fitting curve indicates an overall increase in vessel diameter *ex vivo*, however, capillaries seem to follow and opposite trend. n=50. (d) Comparison of vessel length. The slope value of the fitting curve, along with the high correlation coefficient, indicates a high preservation of vessels length, both for short and long segments. n=10.

Gel-BSA-TRITC + anti-endomucin-FITC   Gel-BSA-TRITC + Gel-BSA-FITC
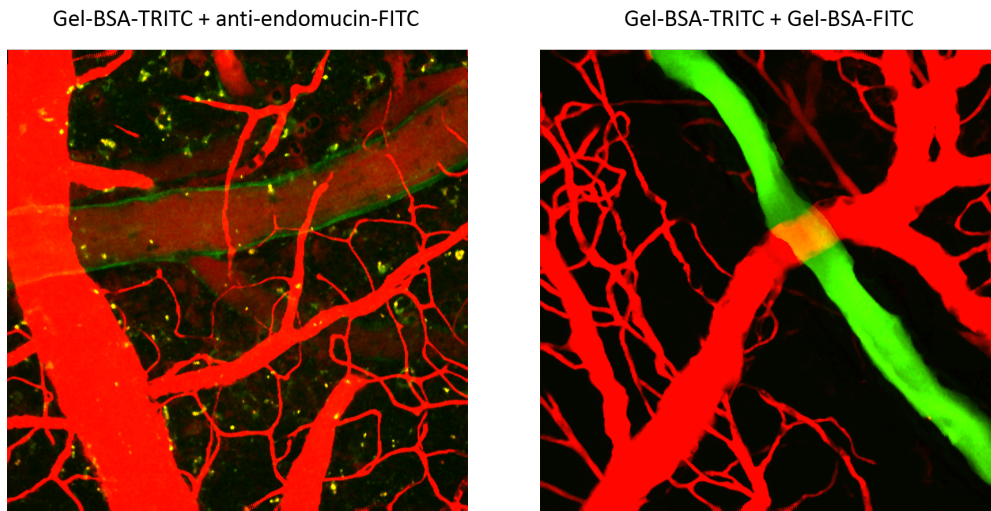
Figure 7.8: **Differential staining of arteries and veins** (left) Anti-endomucin-FITC conjugate (green) is injected before Gel-BSA-TRITC (red) injection. It results in red staining of whole vessels lumen and green staining of veins endothelium. (right) After Gel-BSA-TRITC (red) staining, a small quantity of Gel-BSA-FITC (green) solution is injected. Veins appear red, while arteries, which lie upstream with respect to veins, are filled with Gel-BSA-FITC and appear green. However, the accuracy of this unspecific staining has to be carefully evaluated.

aspecific and differences in the length of the arterial path between mice and/or in different parts of the same brain can produce wrong data. A careful evaluation of both methods has to be performed to verify their reliability.

Chapter 8

Blood vessel analysis with TPFM

Before moving forward to whole brain imaging, the potential of the staining method used was tested for the evaluation of vascular remodeling using TPFM. Contrary to whole brain imaging with LSFM, TPFM does not require tissue clearing. However, in fixed non cleared specimens, imaging is limited to roughly 200 μm in depth. To further expand the depth achievable, a fast clearing procedure described in Costantini et al. [9], consisting in serial incubations of TDE/PBS solutions, was adopted. Although this clearing procedure is not suitable for whole brain, tissue clearing of brain slices is performed in a few hours without the need of specialized devices, which represents an advantage over tissue transformation. The staining procedure described in the previous chapter, in combination with TDE clearing, proved to be a fast and valid methodology for analysis of brain vasculature in confined regions of interest with TPFM.

8.1 Vascular remodelling in a mouse model of stroke

Morphological changes to brain vasculature were evaluated in a photothrombotic model of stroke. This model involves the systemic administration of a light-sensitive dye that can be rapidly and reliably photoactivated, leading to localized damage in a specific area of the brain cortex in a relatively noninvasive manner. One month after the photothrombotic damage, vascular remodeling was evaluated.
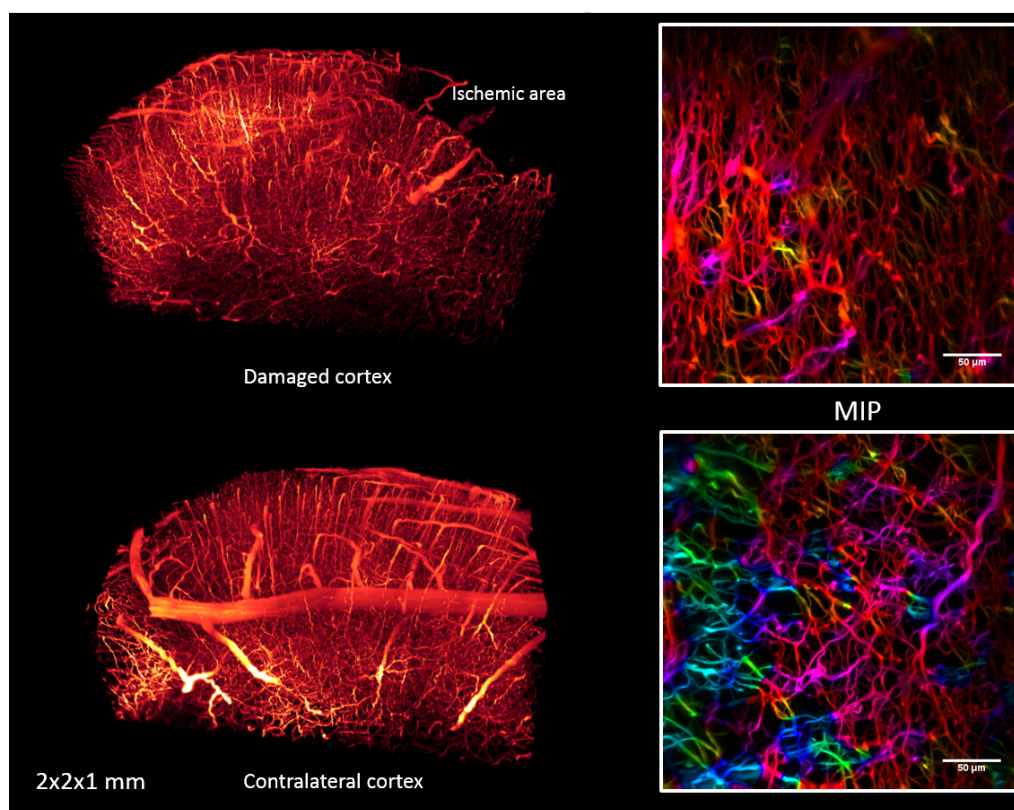
Figure 8.1: **Vessel orientation after stroke** (left) 3D rendering of damaged (upper image) and intact (lower image) cortical region. Two-photon images were stitched with TeraStitcher software and 3D rendered with Amira software. (Right) MIP of 160 μm showing vessels orientation by color code. Red color in the upper image indicates a preferential orientation towards the ischemic region.

As a control group, mice not subjected to cortical damage were used. Imaging of the caudal region adjacent to the stroke was preformed with TPFM on dissected cortex cleared with TDE 63% in PBS. From the images acquired, blood vessels orientation was first investigated using the imageJ plugin orientationJ (fig 8.1).

In the control group, the analysis of vessel orientation showed an even distribution in all directions (fig. 8.2a). One month after stroke, there is a strong orientation towards the lesion within 500 μm from the core of the damage (fig 8.2b,). A less strong orientation towards the damaged core was observed also in distal areas located 1 to 1.5 mm away from the ischemic region (fig. 8.2c).

Investigations on changes in blood vessels density were carried out in
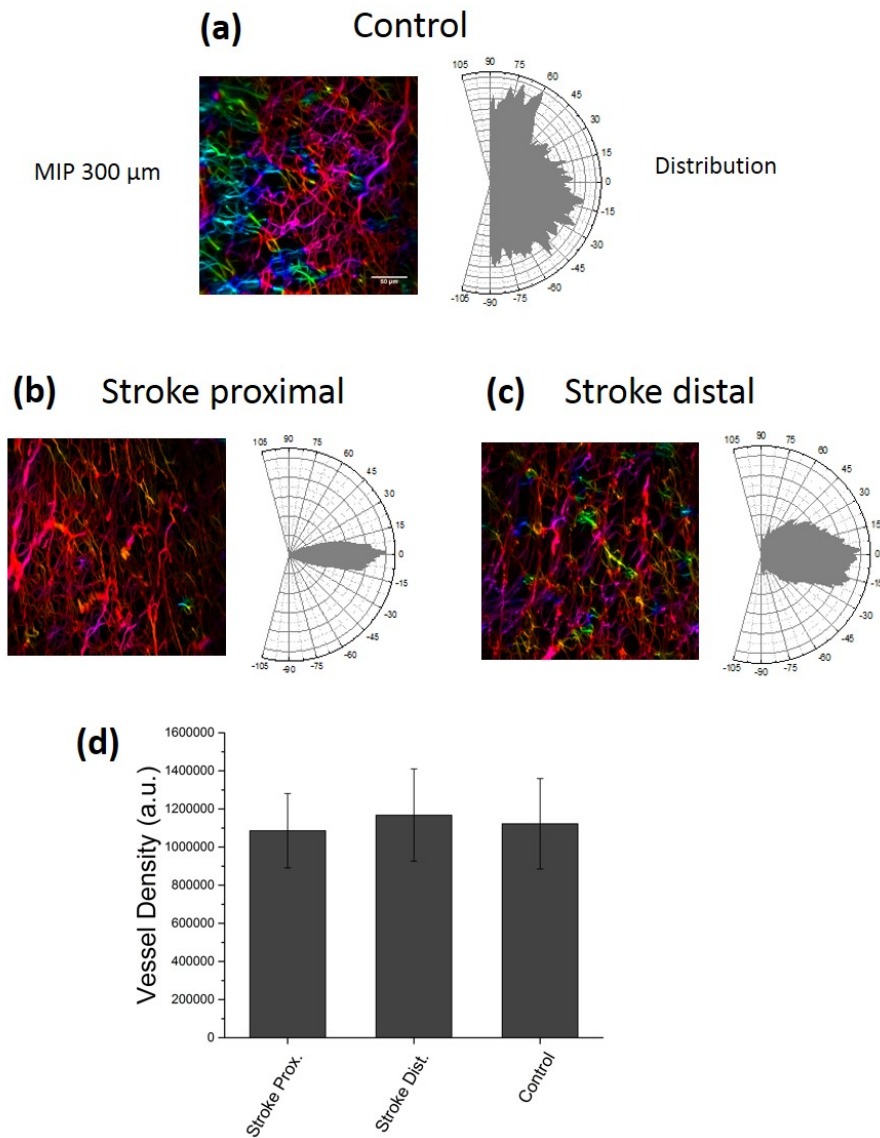
Figure 8.2: **Blood vessels analysis** (a - c) MIPs flanked by polar plots showing the orientation of the vasculature. The color code of the MIPs indicate different orientations. Red color in b and c depict vessels orientated towards the lesion. (a) Control group. (b, c) Stroke group. (d) The pixel counts of binarized image stacks were used as a measure of vessel density. No statistically differences in vessel density were found in the periinfartic region in animals affected by stroke with respect to the control group. n=12, s.d.

addition to vessels orientation. In order to perform these analysis, threshold based binarization was applied on image stacks, and the pixel count was taken as a value of vessels density. The values found did not show a significant difference with respect to the control group neither in the proximal nor in the distal region. (fig. 8.2d).

Chapter 9

Whole mouse brain tomography with LSFM

The analysis of the vascular staining encouraged the application of this method for imaging of whole cleared mouse brains. Thus, as a subsequent step, whole mouse brain tomographies with LSFM were performed, using wild type or Thy1-GFP-M mice for both neuronal and vascular imaging. In order to analyze whole brain data, image segmentation represents a key step to follow. Image quality is an important factor affecting the results of this step. Sophisticated algorithms able to identify and fix segmentation artifacts [117] are in development. In addition, machine learning strategies have been used for automatic identification of brain structures [114], and could be of help to overcome staining inhomogeneities. Such computational methods, however, require hard image processing, making the segmentation of the whole brain dataset a demanding process. Thanks to the high image contrast provided by the methodology used for vessel staining coupled with tissue clearing, a simple segmentation method based on thresholding was applied as a proof of the high image quality yielded by the proposed pipeline.

9.1   Aquisition of whole brain vasculature datasets with LSFM and image segmentation

With LSFM, the acquisition of a complete dataset of whole mouse brain with microscopic resolution is accomplished in a few hours. The imaging process generates a series of contiguous stacks containing overlapping regions with the neighbours in 3D space. Overlapping regions are needed to stitch the images in three dimensions in order to generate a single file of the whole brain (fig. 9.1), using specialized software capable of dealing with teravoxel-size images [108].

The segmentation of whole mouse brain vasculature is a computationally demanding process. Time and computer performance needed depend, however, on the algorithm used, and the quality of images is a decisive factor for the choice of the segmentation algorithm. A high image quality permits the application of simple segmentation methods, which, for instance, do not need to distinguish different levels of signal/background throughout the whole sample. Sample inhomogeneities would require instead sophisticated algorithms able to correctly adequate the parameters used. Thanks to the elevated image quality and signal to background ratio, a simple thresholding was applied for separating blood vessels from the surrounding space. The result of the thresholding based segmentation method was compared with the original image (fig. 9.2).

9.2   Whole mouse brain vascular and neuronal imaging

Since the imaging modality does not damage or destroy the sample, the methodology offer the possibility to perform consecutive imaging sessions of the same brain for acquisition of datasets of different fluorescently labeled structures, such as vessels and neurons. Whole brain neuronal and vascular tomographies of the same sample were carried out using a Thy1-GFP-M mouse line, in which a subset of neurons express GFP (fig. 9.3). BSA-TRITC was used for gel preparation in order to avoid overlap on the fluorescent emission spectra of the GFP-expressing neurons and vascular marker.
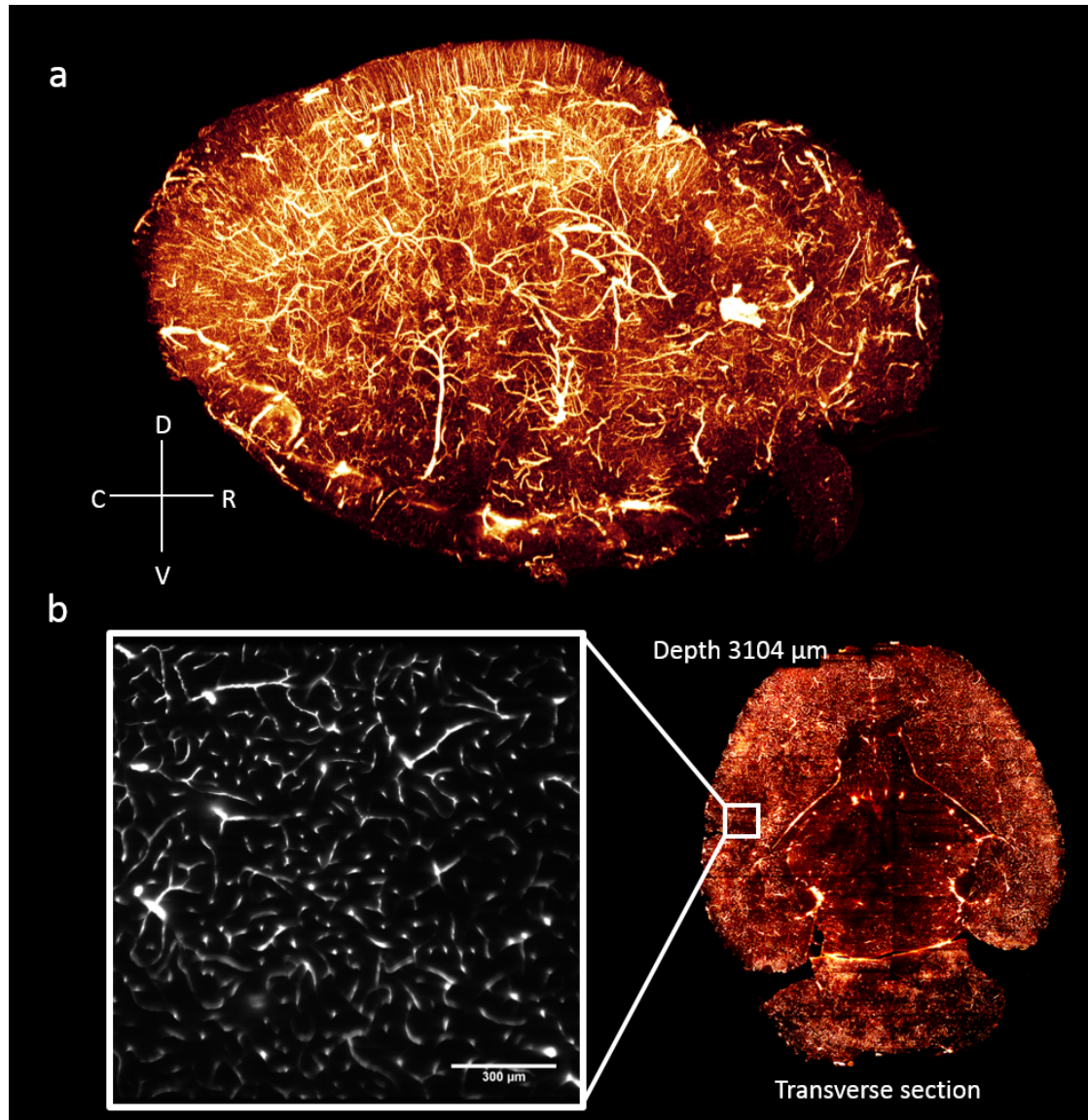
Figure 9.1: **Brain vasculature tomography** (a) 3D rendering showing the whole brain vasculature obtained after stitching. Consecutive stacks acquired with LSFM are aligned and stitched together using the TeraStitcher software. (b) close view of a ROI from a transverse section of the stitched brain. Renderings with Amira software.
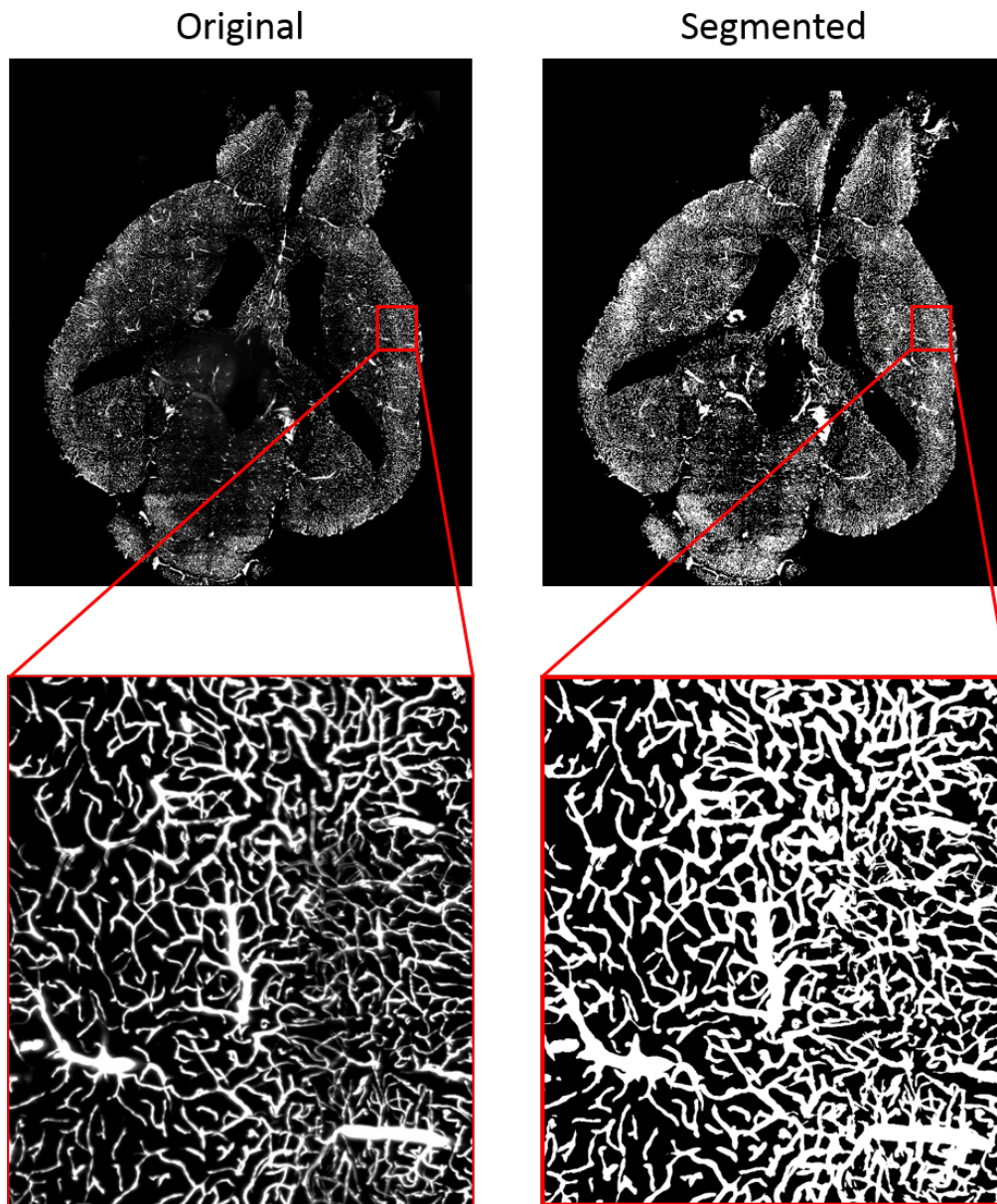
Figure 9.2: **Segmentation of the stitched brain with simple thresholding** (upper) MIPs of transverse sections from the whole stitched brain showing a comparison between original (left) and segmented (right) images. (lower) Close views of a region from the upper images. Thresholding based image segmentation performed with ImageJ.
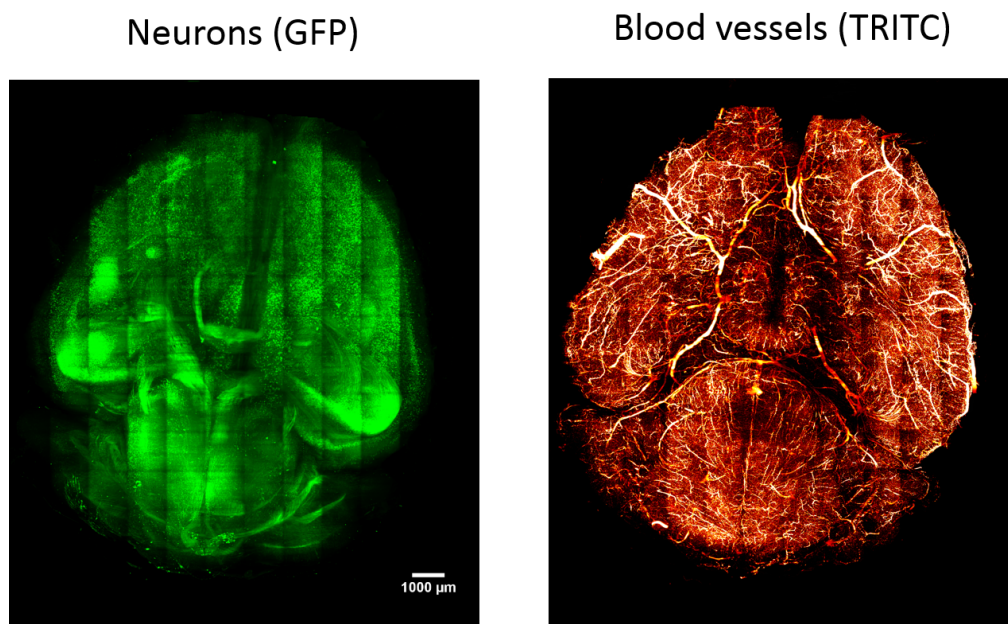
Figure 9.3: **Consecutive whole brain neuron and vessel imaging** Whole brain datasets of GFP-expressing neurons (left) and blood vessels (right) were acquired during consecutive imaging sessions. Both row data were stitched using the TeraStitcher software. MIPs of whole brain optical sections are shown.

Part IV

Conclusions

Chapter 10

Discussion

In the present work, a methodology for whole mouse brain vasculature analysis was presented. The brain vasculature accounts for different sets of vessels, which diameter vary from hundreds of μm for the large cerebral arteries and veins to few microns for the vessels forming the capillary network. Large superficial vessels can be easily detected with a variety of techniques. A fine morphological analysis of the brain vasculature, however, requires a clear visualization of the finest capillaries. The resolution needed for visualizing the capillary network is achievable with optical microscopy. Nevertheless, some constrains limit the applications of optical microscopy for imaging of intact tissues. The main issue is represented by light scattering, which hinders light penetration inside samples. Efforts have been done in the last years in the pursuit to find treatments capable of rendering biological specimens optically transparent, although first clearing approaches date back to one century ago [73]. In parallel we have witnessed the rebirth of another one-hundred old technique, the LSFM. The peculiarity of LSFM allows for whole mouse brain imaging in just a few hours, while keeping a sub-cellular resolution. LSFM, however, is compatible only with transparent samples. Hence, the first step consist on establishing an efficient clearing methodology. Among the clearing approaches proposed in literature, CLARITY [80] seems to be the best choice in term of transparency achievable and fluorescence preservation. However, the very expensive mounting medium FocusClear$^{\text{TM}}$, presented in the CLARITY protocol, limits its use for routinely application and represents a constrain for a

proper characterization of brain vasculature both in physiological and in pathological conditions. This problem has been addressed by replacing FocusClear™ with a TDE/PBS solution [9]. CLARITY-TDE was then chosen as preferred clearing procedure for whole brain imaging in this work.

The second issue concerns vascular staining. Previous works showing whole brain vasculature imaging with LSFM used fluorophore-labeled lectins, which are molecules able to bind sugars present on the endothelium. As a result, only the endothelial walls of blood vessels is labeled, leaving the internal lumen devoid of fluorescence. A staining capable of filling the blood vessels lumen and compatible with CLARITY was therefore established. Comparative analysis showed the advantages of the use of a fluorescent gel over the use of lectin-fluorophore conjugate. First of all, a greater signal is detected, which results in an higher signal to background ratio and consequently an improved image quality over depth. The higher signal permits an easier discrimination of blood vessels from the surrounding space by automatic algorithms for image segmentation. Comparison among MIPs at different depths of segmented images showed an important loss of blood vessels upon automatic segmentation of the Lectin-stained sample with respect to a manual segmentation. The staining of vessel lumen with gelatin permits instead a considerable improving. Superimpositions between automatically and manually segmented stacks, the last assumed as ground truths, showed a greater overlap coefficient for Gel-BSA-FITC stained samples, especially in deep regions. An accurate automatic segmentation is a key step for a topological reconstruction of the vasculature in the whole brain. The large amount of data derived from whole organ imaging can indeed only be processed with automatic tools.

Alterations to the vascular network can lead to spurious results. To verify possible morphological changes due to the staining procedure, a comparison between *in vivo* and *ex vivo* imaging of the same region was carried out. As a result of this investigation, the overall topology appeared well maintained, although changes on blood vessels diameter were detected. However, it is worthy to keep in mind that in physiological conditions the blood vessels size undergo constant changes depending on brain region activity, a process known as neurovascular coupling [12]. On the contrary, the creation of a map representing the vascular network can be addressed in a reliable fashion with this methodology, since the length of vessel

segments resulted preserved after staining.

The vascular network is composed of a set of arteries and a set on veins connected by capillaries. In the presented work, two different approaches were suggested for a clear distinction of the arterial and venular component. The establishment of a reliable differential staining for arteries and veins would permit an easier comprehension of the arterial and venular routes inside the brain.

TPFM imaging showed a possible application on a pathological model of vascular impairment. When the region of interest is confined to a small volume, a simple and fast clearing procedure can be applied, however whole brain analysis are feasible only on completely transparent samples with LSFM. The combination of Gel-BSA-FITC staining with CLARITY-TDE method for tissue clearing offer an improved image quality for LSFM investigation with respect to previous approaches using fluorescent lectins, facilitating the application of automatic tools for whole brain analysis.

LSFM allow non destructive investigation of whole organ. Samples are kept intact and are available for possible future examinations. Furthermore, different structures can be analyzed in the same sample without the need of an imaging apparatus capable of simultaneous distinction of separated fluorescent signals. This feature give for instance the possibility to consecutively investigate the vascular component and the neuronal circuitry using transgenic mouse lines expressing fluorescent proteins inside neurons. On the contrary, serial sectioning methodology negates the possibility of future inspections of the same specimen after imaging.

The applicability of tools for image segmentation was also shown. This is a key step for subsequent analysis and vascular network reconstruction in whole brain. Detailed information of vascular network anatomy is required for understanding several aspects of microcirculation, including regulation of blood flow, oxygen and nutrients transport, and interpretation of hemodynamically based functional imaging methods. Clarifying these aspect is important for a better interpretation of diagnostic tools used for vascular inspection. Similarly, cerebral vascular diseases phenotypes can be defined from a systematic analysis of multiple specimens of pathological models. A robust characterization of morphological alterations found in specific pathologies, as well as the determination of physiological variations, require the analysis of a vast amount of samples. Thus, fast sample preparation

and imaging modality are crucial for obtaining the volumes of data needed in a reasonable time. In the present work, LSFM is used as imaging technique, which achieve complete mouse brain tomography in few hours. The clearing procedure adopted here consist of a passive removal of lipids, which required one month for a single sample, but with the possibility of preparing multiple samples in parallel, since no specific device are needed. However, with recent advancements in the clearing protocol and the implementation of a commercially available device for electrophoretic tissue clearing, a complete transparency can be obtained in few days.

Chapter 11

Future perspective

The acquisition of whole mouse brain datasets with micrometric resolution is the first step for a complete comprehension of the vascular architecture. The analysis of this data is not trivial and require a powerful computer technology. A single brain vascular dataset acquired with LSFM accounts for Terabytes of data. Robust algorithms capable of dealing with such amount of informations, and dedicated computer platforms, are needed for retrieving morphological informations from the raw dataset. An accurate evaluation of the processed data is necessary for avoiding generating wrong results. Future informatics developments will help to obtain more reliable information through an automatic individuation and interpretation of possible imperfections present in the raw dataset. Machine learning approach are likely to be the best choice for accomplishing this task. Algorithms able to recognize and fix staining inhomogeneities are in development and represent an important resource for more accurate analysis [117].

Whole mouse brain vascular analysis of multiple samples will generate a database from which will be possible extracting morphological information about physiological variability. The collection of databases relating to cerebral pathologies will instead allows for the identification of cerebral vascular diseases phenotypes, enhancing our knowledge about brain vascular alterations associate to specific pathologies. Vascular changes have, for instance, an essential role in the regenerative process occurring after stroke. Furthermore, mechanisms involved in neuronal and vascular wiring share deep similarities [118]. This suggests that beyond the

role of providing oxygen and nutrient, molecular messages coming from blood vessels may act as clues for neuronal rewiring. Topological studies of the vascular network can then provide substantial informations about the mechanisms occurring during the regeneration process after brain damages. Associations between studies on functional recovery, with morphological analysis of the vasculature, will also provide a better understanding of this processes.

In cancer, the creation of new vessels from the existing network (angiogenesis) represent an important pathogenic event for cancer growth and metastatic process [119]. Drugs inhibiting angiogenesis are used for cancer therapy and others are in development. It is also known that the level of vascular perfusion can predict response or outcome in patients treated with anti-angiogenic agents. Imaging techniques permitting inspection of vascular morphology may provide further and important predictive information on both experimental and approved therapies.

Also Alzheimer's disease (AD), one of the most common cause of cognitive impairments in elderly, include vascular alterations in its pathophysiological mechanisms, and the role of vascular pathologies as a factor contributing to AD is a topic of current interest [120]. Epidemiological studies have shown that AD and cerebral vascular diseases share common risk factors, suggesting additive or synergistic effects of both pathologies on cognitive decline.

A detailed characterization of the brain vascular network will have a positive impact also for a correct interpretation of functional imaging techniques, such as BOLD-fMRI. This technique reveal changes on the oxygenation level in venous blood as endogenous contrast for visualizing brain areas with increased cerebral activity [121]. Larger veins, often have higher signal than smaller venules and capillaries. This lead to inaccurate localization of the cerebral regions in which changes in neural activity occur. High-resolution vascular imaging, capable of detecting the finest vessels, provide investigators with a tool to examine the relationship between fMRI signal and vascular structures. In order to perform these analysis, an accurate automatic method for vascular segmentation and vectorization is needed. Furthermore, it is necessary that the data yield by the vectorization process contain precise informations about the vessels diameter in addition to the track of the vasculature network. Measurements of microvascular geometry and oxygen distribution *in vivo* in rodents has been performed with TPFM in order to

retrieve physiological informations in association with the BOLD signal [122]. A greater comprehension of the areas associated with the signals detected will allow more accurate spatial mapping of brain responses. In this context, techniques allowing imaging of the vascular network with micrometric resolution in whole brain modality, will give important help, along with functional studies, for a correct interpretation of the data gained from BOLD-fMRI.

Bibliography

[1] H. Markram. The blue brain project. *Nat Rev Neurosci*, 7(2):153–60, 2006.

[2] O. Sporns, G. Tononi, and R. Kotter. The human connectome: A structural description of the human brain. *PLoS Comput Biol*, 1(4):e42, 2005.

[3] https://www.humanbrainproject.eu/.

[4] http://www.braininitiative.nih.gov/.

[5] H. Okano, A. Miyawaki, and K. Kasai. Brain/minds: brain-mapping project in japan. *Philos Trans R Soc Lond B Biol Sci*, 370(1668), 2015.

[6] J. DeFelipe. The anatomical problem posed by brain complexity and size: a potential solution. *Front Neuroanat*, 9:104, 2015.

[7] A. Li, H. Gong, B. Zhang, Q. Wang, C. Yan, J. Wu, Q. Liu, S. Zeng, and Q. Luo. Micro-optical sectioning tomography to obtain a high-resolution atlas of the mouse brain. *Science*, 330(6009):1404–8, 2010.

[8] T. Ragan, L. R. Kadiri, K. U. Venkataraju, K. Bahlmann, J. Sutin, J. Taranda, I. Arganda-Carreras, Y. Kim, H. S. Seung, and P. Osten. Serial two-photon tomography for automated ex vivo mouse brain imaging. *Nat Methods*, 9(3):255–8, 2012.

[9] I. Costantini, J. P. Ghobril, A. P. Di Giovanna, A. L. Allegra Mascaro, L. Silvestri, M. C. Mullenbroich, L. Onofri, V. Conti, F. Vanzi, L. Sacconi, R. Guerrini, H. Markram, G. Iannello, and F. S. Pavone. A versatile clearing agent for multi-modal brain imaging. *Sci Rep*, 5:9808, 2015.

[10] R. Tomer, L. Ye, B. Hsueh, and K. Deisseroth. Advanced clarity for rapid and high-resolution imaging of intact tissues. *Nat Protoc*, 9(7):1682–97, 2014.

[11] H. U. Dodt, U. Leischner, A. Schierloh, N. Jahrling, C. P. Mauch, K. Deininger, J. M. Deussing, M. Eder, W. Zieglgansberger, and K. Becker. Ultramicroscopy: three-dimensional visualization of neuronal networks in the whole mouse brain. *Nat Methods*, 4(4):331–6, 2007.

[12] D. Attwell, A. M. Buchan, S. Charpak, M. Lauritzen, B. A. Macvicar, and E. A. Newman. Glial and neuronal control of brain blood flow. *Nature*, 468(7321):232–43, 2010.

[13] D. Lapi and A. Colantuoni. Remodeling of cerebral microcirculation after ischemia-reperfusion. *J Vasc Res*, 52(1):22–31, 2015.

[14] A. B. Hjelmeland, J. D. Lathia, S. Sathornsumetee, and J. N. Rich. Twisted tango: brain tumor neurovascular interactions. *Nat Neurosci*, 14(11):1375–81, 2011.

[15] E. P. Meyer, A. Ulmann-Schuler, M. Staufenbiel, and T. Krucker. Altered morphology and 3d architecture of brain vasculature in a mouse model for alzheimer's disease. *Proc Natl Acad Sci U S A*, 105(9):3587–92, 2008.

[16] S. Herculano-Houzel. The human brain in numbers: a linearly scaled-up primate brain. *Front Hum Neurosci*, 3:31, 2009.

[17] https://www.wikis.engrade.com/theneuroncell/.

[18] Jessell T.M. Kandel E.R., Schwartz J.H. *Principles of neural science*. Number 4th ed in Principles of neural science 4th ed. McGraw-Hill, 2000.

[19] M. W. Barnett and P. M. Larkman. The action potential. *Pract Neurol*, 7(3):192–7, 2007.

[20] T. Sasaki, N. Matsuki, and Y. Ikegaya. Action-potential modulation during axonal conduction. *Science*, 331(6017):599–601, 2011.

[21] E. D. Gundelfinger and A. Fejtova. Molecular organization and plasticity of the cytomatrix at the active zone. *Curr Opin Neurobiol*, 22(3):423–30, 2012.

[22] Johnson A. Lewis J. Raff M. Roberts K. Alberts, B. and P. Walter. *Molecular biology of the cell*. Number 5th ed in Molecular biology of the cell 5th ed. Garlad Science, 2008.

[23] N. J. Abbott, L. Ronnback, and E. Hansson. Astrocyte-endothelial interactions at the blood-brain barrier. *Nat Rev Neurosci*, 7(1):41–53, 2006.

[24] W. Walz. Role of astrocytes in the clearance of excess extracellular potassium. *Neurochem Int*, 36(4-5):291–300, 2000.

[25] L. Pellerin. How astrocytes feed hungry neurons. *Mol Neurobiol*, 32(1):59–72, 2005.

[26] R. Piet, D. A. Poulain, and S. H. Oliet. Contribution of astrocytes to synaptic transmission in the rat supraoptic nucleus. *Neurochem Int*, 45(2-3):251–7, 2004.

[27] T. Ishibashi, K. A. Dakin, B. Stevens, P. R. Lee, S. V. Kozlov, C. L. Stewart, and R. D. Fields. Astrocytes promote myelination in response to electrical impulses. *Neuron*, 49(6):823–32, 2006.

[28] M. Santello and A. Volterra. Synaptic modulation by astrocytes via ca2+-dependent glutamate release. *Neuroscience*, 158(1):253–9, 2009.

[29] M. A. Anderson, J. E. Burda, Y. Ren, Y. Ao, T. M. O'Shea, R. Kawaguchi, G. Coppola, B. S. Khakh, T. J. Deming, and M. V. Sofroniew. Astrocyte scar formation aids central nervous system axon regeneration. *Nature*, 532(7598):195–200, 2016.

[30] S. Ohata and A. Alvarez-Buylla. Planar organization of multiciliated ependymal (e1) cells in the brain ventricular epithelium. *Trends Neurosci*, 2016.

[31] G. W. Kreutzberg. Microglia: a sensor for pathological events in the cns. *Trends Neurosci*, 19(8):312–8, 1996.

[32] https://mind.ilstu.edu/.

[33] https://www.qbi.uq.edu.au/the-brain/anatomy/brain-lobes/.

[34] S. Shipp. The functional logic of corticostriatal connections. *Brain Struct Funct*, 2016.

[35] R.S. Swenson. *Review of Clinical and Functional Neuroscience*. Dartmouth Medical School, 2006.

[36] R. G. Northcutt. Understanding vertebrate brain evolution. *Integr Comp Biol*, 42(4):743–56, 2002.

[37] J. F. Cryan and A. Holmes. The ascent of mouse: advances in modelling human depression and anxiety. *Nat Rev Drug Discov*, 4(9):775–90, 2005.

[38] R. Faubel, C. Westendorf, E. Bodenschatz, and G. Eichele. Cilia-based flow network in the brain ventricles. *Science*, 353(6295):176–8, 2016.

[39] I. Decimo, G. Fumagalli, V. Berton, M. Krampera, and F. Bifari. Meninges: from protective membrane to stem cell niche. *Am J Stem Cells*, 1(2):92–105, 2012.

[40] K. A. Hossmann. Viability thresholds and the penumbra of focal ischemia. *Ann Neurol*, 36(4):557–65, 1994.

[41] Schwegler J.S. *Anatomia e fisiologia dell'uomo*. Edi.Ermes s.r.l., 1999.

[42] Osborn A.G. *Introduction to cerebral angiography*. Introduction to cerebral angiography. Harper & Row, 1980.

[43] T. H. Murphy and D. Corbett. Plasticity during stroke recovery: from synapse to behaviour. *Nat Rev Neurosci*, 10(12):861–72, 2009.

[44] S. Okuyama, J. Okuyama, J. Okuyama, Y. Tamatsu, K. Shimada, H. Hoshi, and J. Iwai. The arterial circle of willis of the mouse helps to decipher secrets of cerebral vascular accidents in the human. *Med Hypotheses*, 63(6):997–1009, 2004.

[45] M. J. Cipolla. Integrated Systems Physiology: From Molecule to Function. San Rafael (CA).

[46] N. Nishimura, C. B. Schaffer, B. Friedman, P. D. Lyden, and D. Kleinfeld. Penetrating arterioles are a bottleneck in the perfusion of neocortex. *Proc Natl Acad Sci U S A*, 104(1):365–70, 2007.

[47] A. Y. Shih, C. Ruhlmann, P. Blinder, A. Devor, P. J. Drew, B. Friedman, P. M. Knutsen, P. D. Lyden, C. Mateo, L. Mellander, N. Nishimura, C. B. Schaffer, P. S. Tsai, and D. Kleinfeld. Robust and fragile aspects of cortical blood flow in relation to the underlying angioarchitecture. *Microcirculation*, 22(3):204–18, 2015.

[48] https://www.neuroems.com/.

[49] R. C. Crumrine, V. J. Marder, G. M. Taylor, J. C. Lamanna, C. P. Tsipis, P. Scuderi, Jr. Petteway, S. R., and V. Arora. Intra-arterial administration of recombinant tissue-type plasminogen activator (rt-pa) causes more intracranial bleeding than does intravenous rt-pa in a transient rat middle cerebral artery occlusion model. *Exp Transl Stroke Med*, 3(1):10, 2011.

[50] https://medmedicine.it/articoli/69-neurologia-e-psichiatria/meningi/.

[51] H. Gray. *Anatomy of the Human Body.* 1918.

[52] J.R. Lakowicz. *Principles of fluorescence spectroscopy.* Number v. 1 in Principles of Fluorescence Spectroscopy. Springer, 2006.

[53] Max Born and Emil Wolf. *Principles of optics : electromagnetic theory of propagation, interference and diffraction of light.* Cambridge University Press, Cambridge ; New York, 7th expanded edition, 1999.

[54] E. Hecht. *Optics.* Number 2nd ed. in . Addison Wesley, 1987.

[55] J.B. Pawley. *Handbook of biological confocal microscopy. Language of science.* Number v. 1 in Handbook of biological confocal microscopy. Language of science. Springer, 2006.

[56] M. Göppert-Mayer. Über elementarakte mit zwei quantensrpüngen. *Ann Phys*, 9.

[57] W. R. Zipfel, R. M. Williams, and W. W. Webb. Nonlinear magic: multi-photon microscopy in the biosciences. *Nat Biotechnol*, 21(11):1369–77, 2003.

[58] A. Diaspro, G. Chirico, and M. Collini. Two-photon fluorescence excitation and related techniques in biological microscopy. *Q Rev Biophys*, 38(2):97–166, 2005.

[59] W. Denk, J. H. Strickler, and W. W. Webb. Two-photon laser scanning fluorescence microscopy. *Science*, 248(4951):73–6, 1990.

[60] Y. Chen, C. P. Liang, Y. Liu, A. H. Fischer, A. V. Parwani, and L. Pantanowitz. Review of advanced imaging techniques. *J Pathol Inform*, 3:22, 2012.

[61] F. Helmchen and W. Denk. Deep tissue two-photon microscopy. *Nat Methods*, 2(12):932–40, 2005.

[62] K. Svoboda and R. Yasuda. Principles of two-photon excitation microscopy and its applications to neuroscience. *Neuron*, 50(6):823–39, 2006.

[63] P. J. Keller and H. U. Dodt. Light sheet microscopy of living or cleared specimens. *Curr Opin Neurobiol*, 22(1):138–43, 2012.

[64] P. A. Santi. Light sheet fluorescence microscopy: a review. *J Histochem Cytochem*, 59(2):129–38, 2011.

[65] A. H. Voie, D. H. Burns, and F. A. Spelman. Orthogonal-plane fluorescence optical sectioning: three-dimensional imaging of macroscopic biological specimens. *J Microsc*, 170(Pt 3):229–36, 1993.

[66] P. J. Keller, A. D. Schmidt, A. Santella, K. Khairy, Z. Bao, J. Wittbrodt, and E. H. Stelzer. Fast, high-contrast imaging of animal development with scanned light sheet-based structured-illumination microscopy. *Nat Methods*, 7(8):637–42, 2010.

[67] F. O. Fahrbach, V. Gurchenkov, K. Alessandri, P. Nassoy, and A. Rohrbach. Self-reconstructing sectioned bessel beams offer submicron optical sectioning for large fields of view in light-sheet microscopy. *Opt Express*, 21(9):11425–40, 2013.

[68] S. Kalchmair, N. Jahrling, K. Becker, and H. U. Dodt. Image contrast enhancement in confocal ultramicroscopy. *Opt Lett*, 35(1):79–81, 2010.

[69] L. Silvestri, A. Bria, L. Sacconi, G. Iannello, and F. S. Pavone. Confocal light sheet microscopy: micron-scale neuroanatomy of the entire mouse brain. *Opt Express*, 20(18):20582–98, 2012.

[70] J. Huisken and D. Y. Stainier. Even fluorescence excitation by multi-directional selective plane illumination microscopy (mspim). *Opt Lett*, 32(17):2608–10, 2007.

[71] P. Osten and T. W. Margrie. Mapping brain circuitry with a light microscope. *Nat Methods*, 10(6):515–23, 2013.

[72] D. S. Richardson and J. W. Lichtman. Clarifying tissue clearing. *Cell*, 162(2):246–57, 2015.

[73] W. Spalteholz. *Über das durchsichtigmachen von menschlichen und tierischen präparaten*. Leipzig:S. Hirzel, 1914.

[74] M. W. Klymkowsky and J. Hanken. Whole-mount staining of xenopus and other vertebrates. *Methods Cell Biol*, 36:419–41, 1991.

[75] K. Becker, N. Jahrling, S. Saghafi, R. Weiler, and H. U. Dodt. Chemical clearing and dehydration of gfp expressing mouse brains. *PLoS One*, 7(3):e33916, 2012.

[76] N. Renier, Z. Wu, D. J. Simon, J. Yang, P. Ariel, and M. Tessier-Lavigne. idisco: a simple, rapid method to immunolabel large tissue samples for volume imaging. *Cell*, 159(4):896–910, 2014.

[77] H. Hama, H. Kurokawa, H. Kawano, R. Ando, T. Shimogori, H. Noda, K. Fukami, A. Sakaue-Sawano, and A. Miyawaki. Scale: a chemical approach

for fluorescence imaging and reconstruction of transparent mouse brain. *Nat Neurosci*, 14(11):1481–8, 2011.

[78] M. T. Ke, S. Fujimoto, and T. Imai. Seedb: a simple and morphology-preserving optical clearing agent for neuronal circuit reconstruction. *Nat Neurosci*, 16(8):1154–61, 2013.

[79] T. Kuwajima, A. A. Sitko, P. Bhansali, C. Jurgens, W. Guido, and C. Mason. Cleart: a detergent- and solvent-free clearing method for neuronal and non-neuronal tissue. *Development*, 140(6):1364–8, 2013.

[80] K. Chung, J. Wallace, S. Y. Kim, S. Kalyanasundaram, A. S. Andalman, T. J. Davidson, J. J. Mirzabekov, K. A. Zalocusky, J. Mattis, A. K. Denisin, S. Pak, H. Bernstein, C. Ramakrishnan, L. Grosenick, V. Gradinaru, and K. Deisseroth. Structural and molecular interrogation of intact biological systems. *Nature*, 497(7449):332–7, 2013.

[81] N. Beckmann, R. Stirnimann, and D. Bochelen. High-resolution magnetic resonance angiography of the mouse brain: application to murine focal cerebral ischemia models. *J Magn Reson*, 140(2):442–50, 1999.

[82] C. Y. Lin, M. H. Lin, W. M. Cheung, T. N. Lin, J. H. Chen, and C. Chang. In vivo cerebromicrovasculatural visualization using 3d deltar2-based microscopy of magnetic resonance angiography (3ddeltar2-mmra). *Neuroimage*, 45(3):824–31, 2009.

[83] Z. Starosolski, C. A. Villamizar, D. Rendon, M. J. Paldino, D. M. Milewicz, K. B. Ghaghada, and A. V. Annapragada. Ultra high-resolution in vivo computed tomography imaging of mouse cerebrovasculature using a long circulating blood pool contrast agent. *Sci Rep*, 5:10178, 2015.

[84] C. T. Badea, M. Drangova, D. W. Holdsworth, and G. A. Johnson. In vivo small-animal imaging using micro-ct and digital subtraction angiography. *Phys Med Biol*, 53(19):R319–50, 2008.

[85] C. Demene, E. Tiran, L. A. Sieu, A. Bergel, J. L. Gennisson, M. Pernot, T. Deffieux, I. Cohen, and M. Tanter. 4d microvascular imaging based on ultrafast doppler tomography. *Neuroimage*, 127:472–83, 2016.

[86] J. Yao, L. Wang, J. M. Yang, K. I. Maslov, T. T. Wong, L. Li, C. H. Huang, J. Zou, and L. V. Wang. High-speed label-free functional photoacoustic microscopy of mouse brain in action. *Nat Methods*, 12(5):407–10, 2015.

[87] J. Yao and L. V. Wang. Photoacoustic brain imaging: from microscopic to macroscopic scales. *Neurophotonics*, 1(1), 2014.

[88] E. W. Stein, K. Maslov, and L. V. Wang. Noninvasive, in vivo imaging of blood-oxygenation dynamics within the mouse brain using photoacoustic microscopy. *J Biomed Opt*, 14(2):020502, 2009.

[89] G. Hong, S. Diao, J. Chang, A.L. Antaris, C. Chen, B. Zhang, S. Zhao, P.L. Atochin, D.N.and Huang, K.I. Andreasson, C.J. Kuo, and H. Dai. Through-skull fluorescence imaging of the brain in a new near-infrared window. *Nat phot*, 166(8):723–730, 2014.

[90] P. Zakharov, A. C. Volker, M. T. Wyss, F. Haiss, N. Calcinaghi, C. Zunzunegui, A. Buck, F. Scheffold, and B. Weber. Dynamic laser speckle imaging of cerebral blood flow. *Opt Express*, 17(16):13904–17, 2009.

[91] A. K. Dunn, H. Bolay, M. A. Moskowitz, and D. A. Boas. Dynamic imaging of cerebral blood flow using laser speckle. *J Cereb Blood Flow Metab*, 21(3):195–201, 2001.

[92] V. Kalchenko, D. Israeli, Y. Kuznetsov, and A. Harmelin. Transcranial optical vascular imaging (tovi) of cortical hemodynamics in mouse brain. *Sci Rep*, 4:5839, 2014.

[93] G. J. Goldey, D. K. Roumis, L. L. Glickfeld, A. M. Kerlin, R. C. Reid, V. Bonin, D. P. Schafer, and M. L. Andermann. Removable cranial windows for long-term imaging in awake mice. *Nat Protoc*, 9(11):2515–38, 2014.

[94] S. Sakadzic, J. Lee, D. A. Boas, and C. Ayata. High-resolution in vivo optical imaging of stroke injury and repair. *Brain Res*, 1623:174–92, 2015.

[95] C. E. Brown, P. Li, J. D. Boyd, K. R. Delaney, and T. H. Murphy. Extensive turnover of dendritic spines and vascular remodeling in cortical tissues recovering from stroke. *J Neurosci*, 27(15):4101–9, 2007.

[96] M. Mickoleit, B. Schmid, M. Weber, F. O. Fahrbach, S. Hombach, S. Reischauer, and J. Huisken. High-resolution reconstruction of the beating zebrafish heart. *Nat Methods*, 11(9):919–22, 2014.

[97] G. Scala. Microvasculature of the cerebral cortex: a vascular corrosion cast and immunocytochemical study. *Microsc Res Tech*, 77(4):257–63, 2014.

[98] S. Heinzer, T. Krucker, M. Stampanoni, R. Abela, E. P. Meyer, A. Schuler, P. Schneider, and R. Muller. Hierarchical microimaging for multiscale analysis of large vascular networks. *Neuroimage*, 32(2):626–36, 2006.

[99] T. Krucker, A. Lang, and E. P. Meyer. New polyurethane-based material for vascular corrosion casting with improved physical and imaging characteristics. *Microsc Res Tech*, 69(2):138–47, 2006.

[100] F. Plouraboue, P. Cloetens, C. Fonta, A. Steyer, F. Lauwers, and J. P. Marc-Vergnes. X-ray high-resolution vascular network imaging. *J Microsc*, 215(Pt 2):139–48, 2004.

[101] H. Hashimoto, M. Kusakabe, and H. Ishikawa. A novel method for three-dimensional observation of the vascular networks in the whole mouse brain. *Microsc Res Tech*, 71(1):51–9, 2008.

[102] J. Wu, Y. He, Z. Yang, C. Guo, Q. Luo, W. Zhou, S. Chen, A. Li, B. Xiong, T. Jiang, and H. Gong. 3d braincv: simultaneous visualization and analysis of cells and capillaries in a whole mouse brain with one-micron voxel resolution. *Neuroimage*, 87:199–208, 2014.

[103] H. Gong, S. Zeng, C. Yan, X. Lv, Z. Yang, T. Xu, Z. Feng, W. Ding, X. Qi, A. Li, J. Wu, and Q. Luo. Continuously tracing brain-wide long-distance axonal projections in mice at a one-micron voxel resolution. *Neuroimage*, 74:87–98, 2013.

[104] T. Zheng, Z. Yang, A. Li, X. Lv, Z. Zhou, X. Wang, X. Qi, S. Li, Q. Luo, H. Gong, and S. Zeng. Visualization of brain circuits using two-photon fluorescence micro-optical sectioning tomography. *Opt Express*, 21(8):9839–50, 2013.

[105] P. Blinder, P. S. Tsai, J. P. Kaufhold, P. M. Knutsen, H. Suhl, and D. Kleinfeld. The cortical angiome: an interconnected vascular network with non-columnar patterns of blood flow. *Nat Neurosci*, 16(7):889–97, 2013.

[106] N. Jahrling, K. Becker, and H. U. Dodt. 3d-reconstruction of blood vessels by ultramicroscopy. *Organogenesis*, 5(4):227–30, 2009.

[107] A. Erturk, K. Becker, N. Jahrling, C. P. Mauch, C. D. Hojer, J. G. Egen, F. Hellal, F. Bradke, M. Sheng, and H. U. Dodt. Three-dimensional imaging of solvent-cleared organs using 3disco. *Nat Protoc*, 7(11):1983–95, 2012.

[108] A. Bria and G. Iannello. Terastitcher - a tool for fast automatic 3d-stitching of teravoxel-sized microscopy images. *BMC Bioinformatics*, 13:316, 2012.

[109] G. Feng, R. H. Mellor, M. Bernstein, C. Keller-Peck, Q. T. Nguyen, M. Wallace, J. M. Nerbonne, J. W. Lichtman, and J. R. Sanes. Imaging neuronal subsets in transgenic mice expressing multiple spectral variants of gfp. *Neuron*, 28(1):41–51, 2000.

[110] V. Labat-gest and S. Tomasi. Photothrombotic ischemia: a minimally invasive and reproducible photochemical cortical lesion model for mouse stroke studies. *J Vis Exp*, (76), 2013.

[111] P. S. Tsai, J. P. Kaufhold, P. Blinder, B. Friedman, P. J. Drew, H. J. Karten, P. D. Lyden, and D. Kleinfeld. Correlations of neuronal and microvascular densities in murine cortex revealed by direct counting and colocalization of nuclei and vessels. *J Neurosci*, 29(46):14553–70, 2009.

[112] M. C. Mullenbroich, L. Silvestri, L. Onofri, I. Costantini, M. V. Hoff, L. Sacconi, G. Iannello, and F. S. Pavone. Comprehensive optical and data management infrastructure for high-throughput light-sheet microscopy of whole mouse brains. *Neurophotonics*, 2(4):041404, 2015.

[113] A. Roche, D. Ribes, M. Bach-Cuadra, and G. Kruger. On the convergence of em-like algorithms for image segmentation using markov random fields. *Med Image Anal*, 15(6):830–9, 2011.

[114] P. Frasconi, L. Silvestri, P. Soda, R. Cortini, F. S. Pavone, and G. Iannello. Large-scale automated identification of mouse brain cells in confocal light sheet microscopy images. *Bioinformatics*, 30(17):i587–93, 2014.

[115] S. Y. Kim, J. H. Cho, E. Murray, N. Bakh, H. Choi, K. Ohn, L. Ruelas, A. Hubbert, M. McCue, S. L. Vassallo, P. J. Keller, and K. Chung. Stochastic electrotransport selectively enhances the transport of highly electromobile molecules. *Proc Natl Acad Sci U S A*, 112(46):E6274–83, 2015.

[116] W. Johnson, O. Onuma, M. Owolabi, and S. Sachdev. Stroke: a global response is needed. *Bull World Health Organ*, 94(9):634–634A, 2016.

[117] J. P. Kaufhold, P. S. Tsai, P. Blinder, and D. Kleinfeld. Vectorization of optically sectioned brain microvasculature: learning aids completion of vascular graphs by connecting gaps and deleting open-ended segments. *Med Image Anal*, 16(6):1241–58, 2012.

[118] P. Carmeliet and M. Tessier-Lavigne. Common mechanisms of nerve and blood vessel wiring. *Nature*, 436(7048):193–200, 2005.

[119] N. S. Vasudev and A. R. Reynolds. Anti-angiogenic therapy for cancer: current progress, unresolved questions and future directions. *Angiogenesis*, 17(3):471–94, 2014.

[120] J. Attems and K. A. Jellinger. The overlap between vascular disease and alzheimer's disease–lessons from pathology. *BMC Med*, 12:206, 2014.

[121] J. Goense, Y. Bohraus, and N. K. Logothetis. fmri at high spatial resolution: Implications for bold-models. *Front Comput Neurosci*, 10:66, 2016.

[122] L. Gagnon, S. Sakadzic, F. Lesage, J. J. Musacchia, J. Lefebvre, Q. Fang, M. A. Yucel, K. C. Evans, E. T. Mandeville, J. Cohen-Adad, J. R. Polimeni, M. A. Yaseen, E. H. Lo, D. N. Greve, R. B. Buxton, A. M. Dale, A. Devor,

and D. A. Boas. Quantifying the microvascular origin of bold-fmri from first principles with two-photon microscopy and an oxygen-sensitive nanoprobe. *J Neurosci*, 35(8):3663–75, 2015.

Ringraziamenti

Ringrazio il Prof. Francesco Saverio Pavone per la disponibilità e l'interesse mostrato verso il lavoro di ricerca che ho svolto in questi tre anni di dottorato.

Ringrazio il Dott. Leonardo Sacconi che mi ha guidato nelle varie fasi del mio lavoro.

Un ringraziamento particolare al Dott. Ludovico Silvestri, che mi ha seguito durante il periodo di ricerca nonchè di la stesura della tesi.

Ringrazio il Prof. Paolo Frasconi per la sua preziosa collaborazione.

Ringrazio inoltre tutti i colleghi con i quali ho condiviso lo svolgimento degli esperimenti, tra questi:
la Dott.ssa Anna Letizia Allegra Mascaro, grazie a lei ho potuto ampliare sia le mie conoscenze teoriche che le mie competenze pratiche nel campo delle neuroscienze;
la Dott.ssa Irene Costantini, che mi ha mostrato come eseguire procedure sperimentali fondamentali per il mio progetto di dottorato;
la Dott.ssa Caroline Muellenbroich, per il suo fondamentale contributo alla realizzazione del microscopio a foglio di luce e per i suggerimenti di ortografia, utili per la stesura della tesi in lingua inglese.

Oltre a loro, grazie a tutti i colleghi che hanno reso piacevoli e allegre le giornate in laboratorio.

Infine ringrazio la mia famiglia, che come sempre mi ha sostenuto e trasmesso affetto e serenità.